Modelling the interplay between the gut microbiota and its host : application to the analysis of diet impact on symbiosis

Marie Haghebaert, Béatrice Laroche, Lorenzo Sala, Stanislas Mondot, Joël Doré

Highlights

Modelling the interplay between the gut microbiota and its host : application to the analysis of diet impact on symbiosis

Marie Haghebaert, Béatrice Laroche, Lorenzo Sala, Stanislas Mondot, Joël Doré

- We introduce a mathematical model that integrates the dynamics of the colonic crypt, represents various metabolic bacterial groups, assigns each group a specific sensitivity to inflammation, and incorporates colon flows.
- Building on data analysis we provide a bacterial group framework based on metabolic abilities and sensitivity to inflammation.
- We use our model to assess the impact of diet as function of fiber and protein inputs on different symbiotic biomarkers such as the concentration of oxygen in the lumen or mucus production rate.
- By simulating a pathological scenario, we show that a high protein / low fiber diet has a more negative impact on symbiosis resilience compare to a reference diet (higher fiber and lower protein inputs).

Modelling the interplay between the gut microbiota and its host : application to the analysis of diet impact on symbiosis

Marie Haghebaert[a,b], Béatrice Laroche[a,b], Lorenzo Sala[a,b], Stanislas Mondot[c], Joël Doré[c,d]

[a] *Université Paris-Saclay, INRAE, MaIAGE, Jouy-en-Josas, 78350, France*
[b] *Université Paris-Saclay, INRIA, MUSCA, Palaiseau, 91120, France*
[c] *Micalis Institute, INRAE, AgroParisTech, University Paris-Saclay, Jouy-en-Josas, 78350, France*
[d] *Université Paris-Saclay, MGP, INRAE, Jouy-en-Josas, 78350, France*

Abstract

The health and well-being of a host are deeply influenced by the interactions with its gut microbiota. Diet, especially the amount of fiber intake, plays a pivotal role in modulating these interactions impacting microbiota composition and functionality. This paper introduces a novel mathematical model, designed to delve into these interactions, by integrating dynamics of the colonic epithelial crypt, bacterial metabolic functions and sensitivity to inflammation as well as colon flows in a transverse colon section. Unique features of our model include accounting for metabolic shifts in epithelial cells based on butyrate and hydrogen sulfide concentrations, representing the effect of innate immune pattern recognition receptors activation in epithelial cells, capturing bacterial oxygen tolerance based on data analysis, and considering the effect of antimicrobial peptides on the microbiota. Using our model, we show a proof-of-concept that a high-protein, low-fiber diet intensifies dysbiosis and compromises symbiotic resilience. Our simulation results highlight the critical role of adequate butyrate concentrations in maintaining mature epithelial crypts. Through differential simulations focused on varying fiber and protein inputs, our study offers insights into the system's resilience following the onset of dysbiosis. Despite areas for potential improvement, the present model, while having room for enhancement, offers essential understanding of elements such as oxygen levels, the breakdown of fiber and protein, and the basic mechanisms of innate immunity within the colon environment.

Keywords: Mathematical model, PDE-ODE, Bacterial metabolic functional groups, Colon flows model, Crypt model, Host-microbiota interactions

1. Introduction

The gut microbiota, an intricate and dynamic ecosystem comprising billions of microorganisms, has become the focus of substantial scientific interest in past and recent years [1]. Indeed, it plays a crucial role in various physiological processes, such as metabolism regulation and immune system functioning. Investigating the interactions between the gut microbiota and host cells enables us to delve deeper into understanding how these microorganisms contribute to human health and diseases [2, 3].

The host influences bacterial composition and behavior. The epithelial cells lining the colon undertake various critical functions such as nutrient absorption, mucus secretion, and innate immune regulation to curb bacterial overgrowth [4]. The epithelial mucus layers serve dual functions as protective barrier between epithelial cells and luminal content, and as rich source of glycoproteins. The structure and flow of mucus, together with intestinal transit, can profoundly affect microbial colonization and the overall gut microbiota structure [5]. In return the bacterial ecosystem can stimulate the activation of innate immune receptors on epithelial cells, modulating various epithelial cell functions, including mucus and antimicrobial peptides (AMPs) production or cell turnover [6, 7, 8].

Additionally, the gut microbiota composition and functions are profoundly modulated by the host diet, thereby indirectly impacting its health. Western diets, characterized by high protein consumption and low fiber intake, are associated with less diverse and beneficial microbiota composition [9, 10]. The consequent increase in oxygen concentration in the lumen influences commensal bacterial growth, activity, and spatial distribution [11], as well as it affects the functioning of epithelial cells [12]. Conversely, healthier diets, such as the Mediterranean one, which is rich in dietary fibers, foster a more diverse and health-promoting gut microbiota [13, 14]. High fiber intake supports the growth of beneficial bacteria capable of producing short-chain fatty acids (SCFAs), like butyrate. Butyrate acts as the primary energy source for differentiated epithelial cells, exhibits anti-inflammatory properties, and contributes to maintaining the gut barrier [15, 16, 17, 18].

Various experimental approaches, such as germ-free animal models and *in vitro* organoid cultures, have been utilized to study host-microbiota interactions. However, these methods present certain limitations, including reduced complexity and lack of physiological context, which can limit our comprehension of intricate *in vivo* interactions. To fill these gaps, mathematical models serve as a robust platform for hypothesis generation and validation [19].

A range of models have been formulated to elucidate different aspects of this dynamic relationship. For instance, geometric colon models representing bacterial interactions consider various factors such as microbial growth, competition, and environmental conditions in the colon [20, 21]. Others like [22, 23, 24] focused on the representation of bacterial communities while providing a simple physical description of the colon. None of them include the epithelium dynamics while it is directly in interactions with the microbiota and colon physiological mechanisms. A colonic crypt model, proposed by [25] encapsulates the dynamics

of epithelial cell differentiation and proliferation, and the influence of the butyrate and oxygen diffusion within the crypt. In the latter, microbiota presence is only evoked by butyrate presence. To explore the impact of innate immunity reactions researchers have developed model to investigate the activation of innate immunity receptors in the gut [26], pathogen invasion and antimicrobial peptide production [27], receptor activation by specific bacteria [28], and to incorporate adaptive immune system components to study allergy development [29].

The model described here focuses on the dynamic of the colonic crypt, metabolic functional and inflammation response-based bacterial groups, and colon flows within a transverse colon section. This approach facilitates novel insights into host-microbiota interactions and their impact on human health. The crypt dynamics stems from the model proposed in [25], extending the description in order to include new metabolites diffusion and absorption, and the concept of switch in differentiated cell metabolism depending on butyrate and hydrogen sulfide concentrations. Our functional-based modelling of the microbial community draws upon [21] and [20] and takes inspiration from the recent paper [30], where a process-based modelling of the gut microbiota is established. Compared to the functional organization proposed in[21], we added dietary protein input and degradation by a new functional bacterial group comprising sulfate-reducing bacteria and those capable of catabolizing cysteine. We represent the basal innate immunity response at the mucosal surface and its influence on cell division, mucus and AMPs production, essential factors for symbiosis, and account for dietary impact by varying fiber and protein intakes. Furthermore, we address the influence of oxygen concentrations on the system's behavior, thereby offering new perspectives on the intricate host-microbiota relationship. We place the model on a section of the colon to bridge the gap between crypt and colon scale.

To our knowledge, this model is the first to simultaneously study colonic crypt dynamics, mucus, innate epithelial response, fiber and protein degradation by functional bacterial groups, and oxygen diffusion in the environment. Its description is given in section 2. Simulation issues such numerical methods, scale differences and computational time considerations are addressed in section 3. We show the ability to simulate a healthy state in section 4. Then the model is used to investigate diet effects by simulating different fibers and protein inputs on symbiosis biomarkers. By mimicking a breach in the epithelial barrier, we assess symbiotic resilience under a high protein / low fiber diet. Section 5 is devoted to a discussion on the hypothesis underlying this work and addresses perspective works.

2. Model development

Our model represents bacterial metabolism with fiber and protein breakdown by bacterial groups. Thanks to a data analysis, in which we created clusters of bacteria based on their sensitivity to inflammation, we were able to introduce a representation of bacteria that links metabolic abilities and sensitivity to inflammation. The model also encompasses volumes flows in the colon, innate immunity mechanisms at the epithelium scale, epithelial metabolism and the dynamics of colonic crypt. In this section we introduce our modelling choices as well as the data analysis we conducted. Fig. 1 summarizes all interactions between the host and the gut microbiota included in our model.

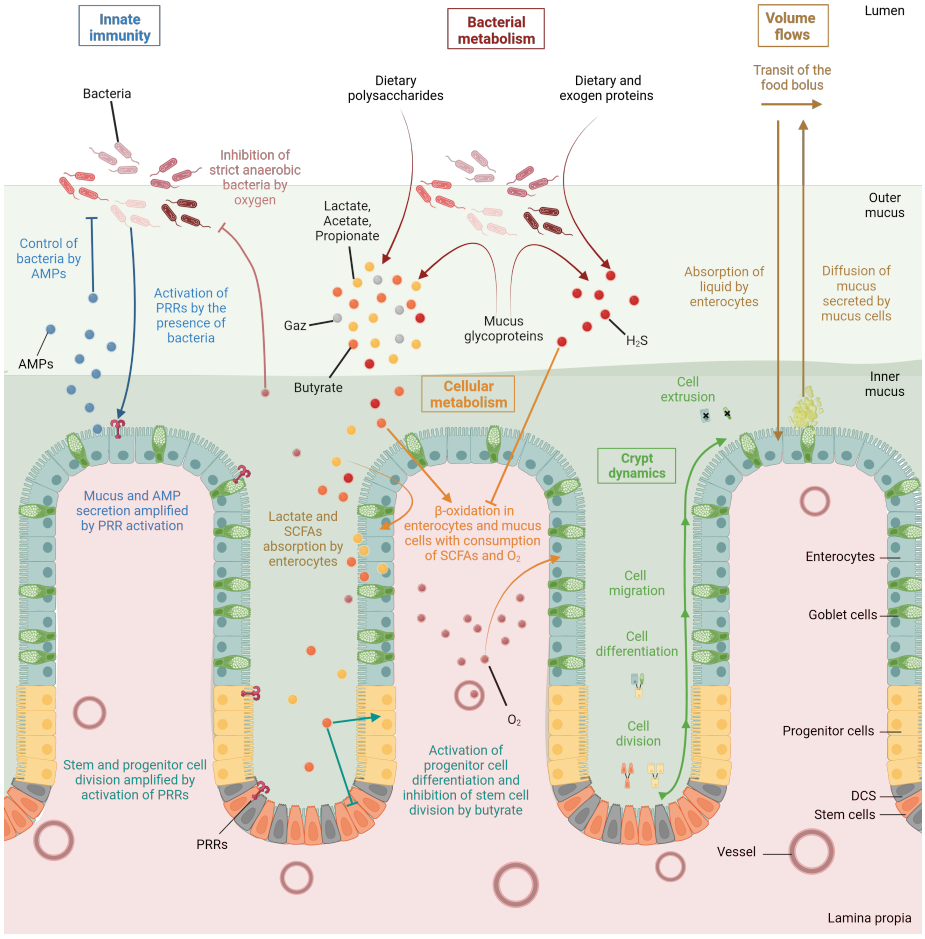

Figure 1: **Biological representation of the main symbiotic mechanisms present in our model**.Created with Biorender.com

2.1. Microbiota model integrating metabolic functions and sensitivity to inflammation

Metabolic functions refer to the suite of biochemical reactions performed by the bacteria, including nutrient uptake, growth, and waste product excretion. While sensitivity to inflammation refers to how different bacterial species react to inflammation in the colon, this involves varying degree of survival, growth reduction, or even death. Combining these two aspects in a single model is a complex task due to their interdependence and dynamic nature.

2.1.1. Metabolic process-based bacterial groups

Our model includes five metabolic bacterial groups responsible for polysaccharide and protein degradation. This group-based approach leverages metabolic redundancy among bacterial species for efficiency.

Polysaccharide degradation. Well described in [21] the fermentative breakdown of polysaccharides involves multiple bacterial groups interconnected by trophic relationships.

First, B_{mon}, is a functional group with the ability to hydrolyze polysaccharides and mucopolysaccharides, resulting in the generation of monosaccharides as end products. After hydrolysing polysaccharides, B_{mon} metabolizes the resultant monosaccharides to fuel its growth. This later process is accompanied by lactate and SCFAs production, specifically acetate, propionate, and butyrate. It also generates gases, predominantly hydrogen (H_2) and carbon dioxide (CO_2).

The second group, denoted as B_{la}, utilizes lactate to facilitate its growth. In the process, it produces SCFAs, H_2, and CO_2. Within the B_{la} group, we propose to distinguish between two metabolic pathways: oxidative and fermentative. Notably, the oxidative pathway involves oxygen consumption.

Then groups B_{H_2a} and B_{H_2m} are hydrogenotrophic microorganismes, they use H_2 and C_{O2} for their energy production. They serve distinct roles as acetogens and methanogens, respectively resulting in the formation of acetate (in the case of B_{H_2a}) and methane (CH_4, in the case of B_{H_2m}). Methanogenesis is a pH dependent reaction, thus, based on [21], this dependence is modelled through the parameter I_{pH} in the reaction term.

Protein breakdown and hydrogen sulfide production. Building upon the original framework posited by [21], we sought to refine and extend the bacterial representation within the model. Previously, the model accounted for only two hydrogenotrophic microorganismes (acetogens and methanogens). This work has delved into the incorporation of a third category: the sulfate-reducing bacteria (SRB).

SRBs are recognized for utilizing hydrogen to synthesize hydrogen sulfide (H2S), a critical process in interaction of host-microbiota. Indeed, in moderate concentrations, epithelial cells metabolize H_2S, but when the concentration exceeds a certain limit, it becomes toxic, inhibiting β-oxidation. The latter is a cell metabolic process where SCFAs are decomposed to produce energy while consuming oxygen [31]. Moreover, elevated H_2S levels also compromise mucus

bonds, undermining the efficacy of the mucus network [31]. While H2S production is attributed to SRB activity, it is also significantly generated through cysteine catabolism [31], a constituent amino acid of proteins.

To address H_2S production, we have introduced a novel bacterial group within our model, the B_{H_2s} group, with proteins, H_2, and CO_2 acting as fuel for growth and leading to the synthesis of H_2S [32]. This group encompasses not only SRB but also those bacteria capable of cysteine catabolism. The integration of this group enables the model to account for the presence of protein within the colonic environment. While they are less abundant in the dietary content than fibers, due to their breakdown in the small intestine, proteins can still find their way to the colon especially under high-protein diets [9].

Several facultative anaerobic bacteria, such as *Escherichia*, *Salmonella*, *Streptococcus*, and *Enterobacter*, contribute to H_2S production [31]. We suggest that B_{H_2s}, like these bacteria, utilizes an oxidative metabolic process consuming O_2. This oxidative metabolism is more energy-rich than fermentative processes, affording B_{H_2s} a higher division rate compared to polysaccharides-degrading groups. It's worth noting that B_{H_2s} can degrade proteins, conferring mucolytic properties upon the group. Yet, we set the hypothesis that mucoprotein degradation is less energy-efficient than that of dietary proteins, resulting in slower division and less H_2S production.

In our microbial metabolism representation, B_{H_2s} group serves as our metaphorical 'villain,' due to its cytotoxic H_2S production and its ability to thrive in an oxygen-rich environment.

To summarize, the model includes 5 distinct metabolic process-based bacterial groups, each involved in various stages of polysaccharides and proteins degradation pathways (Fig. 2).

2.1.2. Refined bacterial groups based on sensitivity to inflammation

Inflammatory response is the first immune reaction of the host to protect itself from the gut microbiota. Bacteria are not all equally sensitive to inflammation, some can benefit from this state while others can be seriously threatened. Our approach is to propose a bacterial representation combining both, metabolism abilities and sensitivity to inflammation. By conducting a time-curve analysis of bacterial populations in rats subjected to inflammation-like perturbations, we aim to discern distinct bacterial responses to inflammation and associate them with the metabolic process-based bacterial groups defined earlier. The data we use are 16S rRNA gene sequencing data counts generated by the bioinformatic processing of sequencing data available under BioProject PRJNA986321.

Temporal curves clustering. Our methodology employs curve clustering to group bacterial genera based on their proportional temporal behavior across individual rats. Rats were subjected to three doses of Dextran Sulfate Sodium (DSS), a compound known to induce gut tissue injury and concomitant inflammation [33], leading to elevated oxygen levels in the gut lumen. There are two groups of rats: group A (10 control rats) and group B (10 rats undergoing DSS treatment).

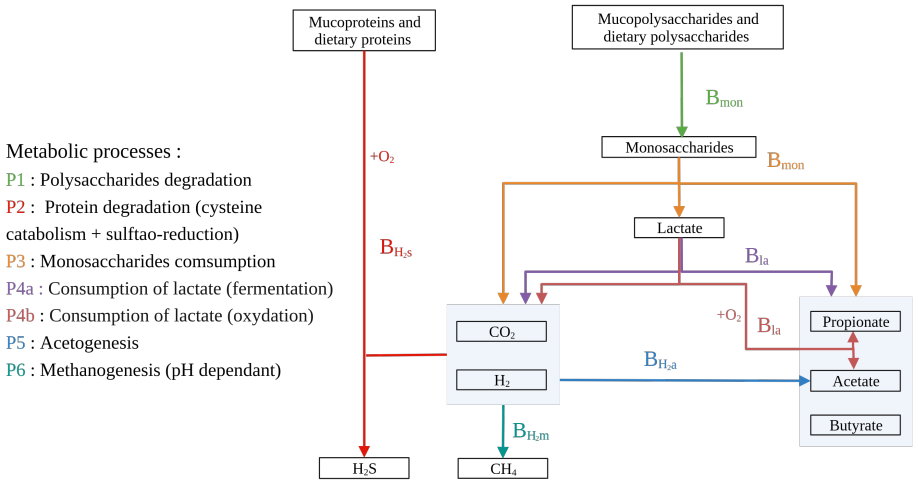

Figure 2: **Metabolic processes representation**. This diagram elucidates the intricate relationships between various bacterial groups that participate in the fermentative degradation of polysaccharides and protein breakdown as depicted in our model. Each metabolic process is designated by a unique number and color. Arrows originate from the reaction substrates and culminate at the end-products, linking them to the corresponding bacterial groups. The term $+O_2$ denotes oxygen consumption and signifies an oxidation reaction. For clarity, we group related end-products within light-blue boxes.

First, in all samples counts were normalized to within sample proportions, in order to ensure consistent between sample comparisons. Based on these proportions, we computed a cosine dissimilarity measure between each two bacterial genera, s_i and s_j according to:

$$D(s_i, s_j) = 1 - \frac{1}{\sum_{h=1}^{H} \omega^h} \sum_{h=1}^{H} \omega^h \frac{s_i^h . s_j^h}{||s_i^h|| \times ||s_j^h||}, \tag{1}$$

Here, H represents the total number of hosts. For a given host h, we denote the number of samples collected by ω^h and use the vectors s_i^h and s_j^h to capture the proportions of the genera s_i and s_j, respectively, within these ω^h samples. To calibrate the influence of each host on the overall dissimilarity measure based on their number of samples, we introduce a weighting by $(\omega^1, \cdots, \omega^H)$. This weighting ensures that hosts providing more samples have a proportionately greater impact on the dissimilarity calculation.

The resulting dissimilarity matrix between bacterial genera was clustered using a Stochastic Block Model (SBM) [34] implemented in the R package 'Blockmodels' [35].

The model was trained on the data from treated rats (group B), yielding $K = 12$ clusters based on the Integrated Completed Likelihood (ICL) criterion for optimal model selection. These clusters were subsequently compared against the control group A. To enhance clarity, we focused on clusters with mean intra-

cluster cosine dissimilarity not exceeding 0.4.

Fig. 3 displays the temporal behavior of each cluster in both groups A and B, with descriptors representing the sum of bacterial species proportions in each cluster in the rats. We provide medians and 95% confidence interval for both groups, and the mean intra-host cosine dissimilarity for each cluster is also given.

To evaluate the statistical significance of differences between groups A and B, we conducted a bilateral Wilcoxon's test at time $T86$, which corresponds to the post-DSS treatment sample in group B. Clusters 1, 4, 5, 6, and 10 exhibited significant differences with a p-value < 0.05 (see Fig 3), their significant phyla and genera composition is illustrated in Fig. 4. Cluster 1, negatively impacted by inflammation, predominantly consisted of *Blautia* and *Akkermansia*, bacteria renowned for acetate and propionate production respectively [36, 37]. Meanwhile, cluster 10, a cluster also impacted negatively by inflammatory state, is composed of bacterial genera known for SCFAs production, with a particular emphasis on butyrate-producing genera such as *Clostridium XIVa* and *Butyricimosa*.

Conversely, clusters 4 and 5 displayed a significantly positive response to inflammation. In particular, cluster 4 housed bacteria proficient in SCFAs and acetate production, underscoring their resilience against inflammatory conditions. In contrast, cluster 5 was characterized by the presence of facultative anaerobic bacteria, notably *Ligilactobacillus* [38], and potential pathobionts such as *Escherichia Shigella* [39].

From this analysis, we observe three levels of sensitivity to inflammation: ϕ for bacteria exhibiting high sensitivity, η for those demonstrating medium sensitivity, and δ for those displaying tolerance or even promotion by inflammation. We now proceed to elucidate how we associate these behaviour with the previously defined metabolic functional groups.

Bacterial groups inflammation sensitivity index. Firstly, in our model we chose the oxygen concentration as our primary marker for inflammation. This choice is underpinned by a correlation: increased inflammation often coincides with a surge in oxygen concentration within the colon [11]. Furthermore, our model encompasses a crypt epithelium component, accounting for oxygen influx from the host vascular system.

With this inflammation marker defined, we have adapted the previously proposed functional bacterial groups to better reflect the observed variation in oxygen tolerance. Specifically, bacteria that consume monosaccharides have been bifurcated into two distinct subgroups based on oxygen tolerance: B^{ϕ}_{mon} and B^{η}_{mon}. A similar distinction has been made for lactate fermenters, designated as B^{ϕ}_{la} and B^{η}_{la}. We have introduced two bacterial groups exhibiting oxidative metabolism: the lactate consumers B^{δ}_{la} and the hydrogen sulfide producers $B^{\delta}_{H_2s}$. Intrinsically, these two groups are believed to be more resilient to inflammation, given their metabolic reliance on oxygen. On the flip side, the bacterial groups $B^{\phi}_{H_2a}$ and $B^{\phi}_{H_2m}$, recognized for their oxygen sensitivity, are directly attributed a heightened vulnerability to inflammatory conditions.

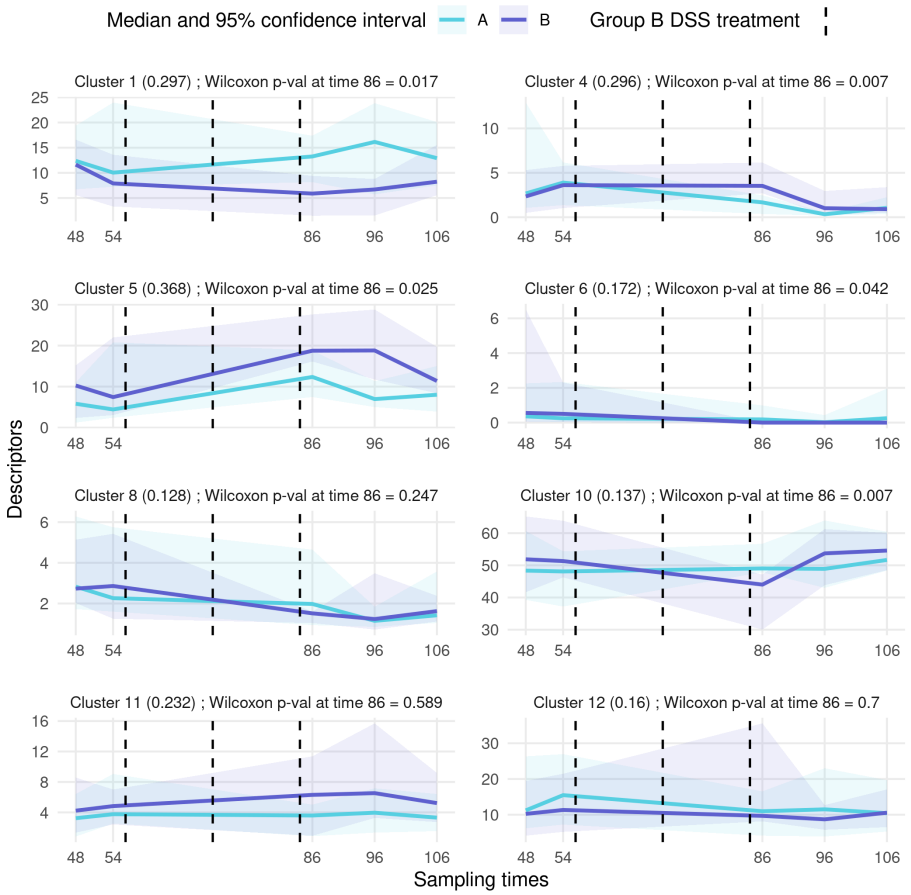

Figure 3: **Cluster behaviors within groups A and B**. For each bacterial genera cluster resulting from SBM, we display its temporal behaviour in group A (control) and in group B (treated). We represent the median and 95% confidence interval of rats within group A and B. Clusters are given with their number and their mean intra-host cosine dissimilarity in brackets. We use a bilateral Wilcoxon test at T86 to evaluate the significance of between group differences after the DSS treatment. The p-values obtained for each cluster are indicated.

Figure 4: **Composition of clusters 1,4,5 and from temporal analysis in rats with DSS-induced inflammation**. For each cluster with a significant difference between control and treated group at time 86 (see Fig. 3) the corresponding composition in term of genera is depicted. Here, for each cluster the mean proportion of the main genera only is represented, we do not explicitly show those with small proportions. A complete figure, with clusters from Fig. 3, is provided in appendix A.19

.

Our refined bacterial representation now captures the complex partition of bacteria according to their metabolic processes and respective response to inflammation.

2.2. Host-physiology modeling

Existing models, as proposed by [21, 20, 30] provide a holistic view of the entire colon. In contrast, our intention is to bridge a comprehensive colon model with the more localized model of epithelial crypt presented in [40]. This necessitates addressing the scale discrepancy between a complete depiction of the colon and the microscopic representation of the epithelial crypt.

To accomplish this, we chose to focus on a small section of the transverse colon, which effectively bridges these different spatial scales, facilitating the dynamic interplay we aim to investigate. This narrow scope enabled us to sidestep the complexity of fluid mechanics, well described in [20], which, while comprehensive, was not particularly relevant to our present exploration.

The transverse colon was chosen as the site of our sectioning for several reasons. It allows avoiding modelling issues related to the periodicity of transit specific to the descending colon, which made it an appealing candidate. Moreover, its higher bacterial density renders it more relevant to our study than the ascending colon.

This selected colon section is modelled using an ordinary differential equation (ODE) compartmental model that is volume-conservative and influenced by both longitudinal and transverse flows. These transverse flows result from the coupling with the crypt model, where the absorption and secretion are modulated by epithelial cells (see Fig. 1. In the following section, we begin by shedding light on the compartmental model and its integration within the comprehensive metabolic and inflammatory response microbial model. We then proceed to present the crypt model and outline the enhancements we propose based on the model in [40].

2.2.1. Compartmental model of colon flows

The colon flows model is located within a section of the transverse colon, which is divided into three volume preserving spatial compartments: the lumen (L), the outer mucus phase (O), and the inner mucus phase (I), gathered in $\mathcal{X} = \{L, O, I\}$ (Fig. 5). Unlike [21, 20], we expand the representation of mucus by differentiating between the outer and inner mucus phases, with the inner phase typically remaining bacteria-free in healthy scenarios. Following the methodology in [20], we leverage mixture theory to delineate the evolution of solid phases, particularly focusing on components large enough to exert mechanical forces. We assume that all phases of the mixture components in the model bear the same density as water and we track the volume fraction dynamics within each compartment. Dissolved components are represented as uniformly distributed concentrations in the compartments as in [20].

The solid components include mucus (m), polysaccharides (pol), proteins ($prot$), dietary residuals (r), liquid chyme (l), and the eight functional bac-

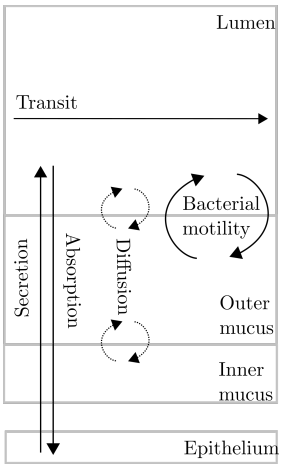

Figure 5: **Schematic representation of flows in the model**. We represent transit, absorption, secretion, diffusion and bacterial motility flows within the model compartments. The Epithelium is depicted by the crypt model. Secretion refers to mucus, antimicrobial peptides (AMPs) and oxygen production, absorption refers to liquid, dissolved metabolites and H_2S. Diffusion is linked to gases ans monosaccharides, bacterial motility is a shortcut for adherence, residence and shear effects and finally transit flow influences all state variables in the lumen compartment.

terial groups denoted as $\mathcal{B} = \{B^{\phi}_{mon},\ B^{\eta}_{mon}, B^{\phi}_{la},\ B^{\eta}_{la}, B^{\delta}_{la}, B^{\delta}_{H_2s},\ B^{\phi}_{H_2a}, B^{\phi}_{H_2m}\}$ presented in 2.1. Solid components are compiled in $\mathcal{V} = \mathcal{B} \cup \{m,\ pol,\ prot,\ r, l\}$.

Dissolved components are gathered in the set $\mathcal{D} = \{\ mon,\ la,\ ac\ ,\ pro,\ but,\ CH_4,\ CO_2,\ H_2,\ H_2S,\ O_2,\ AMPs\}$, symbolizing monosaccharides (mon), lactate (la), acetate (ac), propionate (pro), butyrate (but), methane (CH_4), carbon dioxide (CO_2), hydrogen (H_2), hydrogen sulfide (H_2S), oxygen (O_2), and antimicrobial peptides ($AMPs$). All gases in the model are denoted by $G = \{\ CH_4,\ CO_2,\ H_2,\ H_2S\}$. Oxygen is omitted in this set as we follow [40] strategy to represent it only as a solute concentration. In accordance with [20], we do not directly incorporate the gaseous phase into our model, instead we assume gas concentrations to be at equilibrium with the dissolved phase. This simplification facilitates our focus on the dynamics of solid and liquid phases, see [21] for the representation of gaseous phase.

Governing equations. The core dynamics of the model are governed by a set of ODEs. These equations dictate the time evolution of the state variables, influenced by the diverse flows occurring in the colon and the presence of bacteria.

For each compartment $x \in \mathcal{X}$, the model comprises equations for $f^x_i\ i \in \mathcal{V}$, representing the mixture phase volume fractions, and $c^x_j\ j \in \mathcal{D}$, denoting the concentrations of dissolved elements. These equations are expressed for all $t > 0$ as:

$$\dot{f_i^x}(t) = \sum_{h \in \mathcal{H}} U_h^x[f_i^x(t)] + F_i^x(t) \qquad \text{and} \qquad \dot{c_j^x}(t) = \sum_{h \in \mathcal{H}} U_h^x[c_j^x(t)] + C_j^x(t). \tag{2}$$

Here, $\mathcal{H} = \{T, S, A, D, M\}$ represents the set of modeled flows: transit (T), secretion (S), absorption (A), diffusion (D), and bacterial motion (M). Functions $U_h^x \ \forall h \in \mathcal{H}$ define the form of each of these flows in compartment x. F_i^x and C_j^x represent metabolic transformations applied to the mixture phase and dissolved elements, respectively. These will be elaborated upon in the following sections.

From mass conservation during metabolic processes we have the constraint:

$$\sum_{i \in \mathcal{V}} F_i^x(t) = 0 \ \ \forall t > 0; \ \forall x \in \mathcal{X}. \tag{3}$$

Moreover, considering the mixture theory of volume fractions, we have the following condition:

$$\sum_{i \in \mathcal{V}} f_i^x(t) = 1 \ \forall t > 0 \ \forall x \in \mathcal{X}. \tag{4}$$

Colon section geometry. We use a cylinder form to represent the colon section (Fig. 6). Its shape is given by $L_{sec} = 1cm$ the length and $R = 2.5cm$ the colon radius. Mucus thickness is $e_m = 0.0830cm$ [21]. By concentrating on a small colon section L_{sec}, we assume the lack of longitudinal flows near the gut wall due to the mucus acting as a gel phase. We denote by Γ^{in} the input surface of the lumen compartment and $\Gamma^{out} = \Gamma^{in}$ the output ones, Γ^L and V^L are the exchange surface between the lumen and the outer mucus phase and the lumen volume, Γ^O and V^O the exchange surface between the outer and the inner mucus phases and the outer mucus volume and Γ^I and V^I the exchange surface between the inner mucus phase and the epithelium and the inner mucus volume.

Colon flows definition. Here we define the various flows $U_h \ h \in \mathcal{H}$ in Eq. (2) taking place within the colon section. For the sake of simplicity and clarity in our notations, we have adopted the following conventions:

- We use indices to denote components and solutes.
- Exponents are used to represent compartments.
- The flow velocity are denoted by v, and we use exponents to specify the source and destination compartments for each flow. We list the source compartment first, followed by the destination compartment. If a flow is exchanged between the inner mucus layer and the epithelium, we use E to symbolize the epithelium.

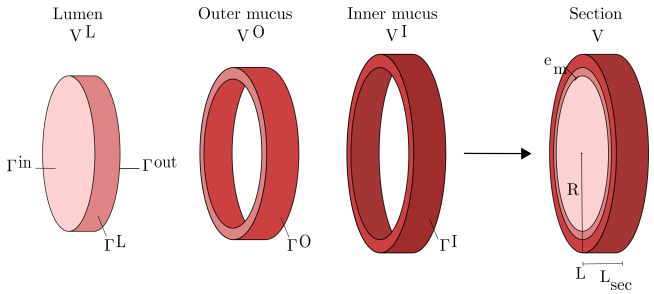

Figure 6: **Diagram illustrating the geometrical representation of the compartmental model of the colon section**. The model consists of three compartments: Lumen, Outer mucus, and Inner mucus, their respective volumes are denoted by $V^x \ \forall x \in \mathcal{X}$. The interface between the Lumen and Outer mucus compartments is denoted by Γ^L, the interface between the Outer mucus and Inner mucus compartments is denoted by Γ^O, and the interface between the Inner mucus and the epithelium is denoted by Γ^I. The total length of the section is L_{sec}, and the radius is R, while the total mucus thickness is e_m. The input and output surfaces of the system are represented by Γ^{in} and Γ^{out}.

Transit flows As a result of the section representation, we only set longitudinal input and output flows v^{in} and $v^{out}(t)$, within the Lumen compartment of the model, where $v_{out}(t)$ is used to ensure constant volume. The transit flow acts on all volume fractions and dissolved components. Only bacteria exhibit a transit resistance capacity, we use the same expression as in [21] to address this ability and denote by τ the bacterial residence time. Using y^{in} as input values, we set :

$$U_T^x[y] = \begin{cases} \frac{\Gamma^{in}}{V^L}\left(v^{in}y^{in} - v^{out}(t)\ y^L\right) & \text{if } x = L \text{ and } y \in \{(f_i)_{i\in\mathcal{V}\setminus\mathcal{B}} \cup (c_j)_{j\in\mathcal{D}}\}, \\ \frac{\Gamma^{in}}{V^L}\left(v^{in}y^{in} - \frac{1}{\tau + \frac{V^L v^{out}(t)}{\Gamma^{in}}} y^L\right) & \text{if } x = L \text{ and } y \in (f_i)_{i\in\mathcal{B}}, \\ 0 & \text{if } x \in \{O, I\}. \end{cases} \tag{5}$$

Because of their volume, polysaccharides (*pol*), proteins (*prot*) and chyme residual (r) cannot enter in the mucus, therefore they are only present in the lumen compartment and undergo only the transit flow [20].

Secretion flows These flows include epithelial crypt-induced flows occurring from the epithelium to the lumen, they are applied to mucus, AMPs, and oxygen.

In the inner mucus compartment mucus and AMPs intake flows depend on goblet and enterocyte cells present in the epithelial crypt. They are produced to protect epithelium from pathogen invasion and they play a vital role in the epithelial barrier efficiency. We model a constant production rate linked to basal cell functioning. With the presence of innate immunity receptors on and in cells : the Pattern Recognition Receptor, cells are able to detect bacteria and respond to their presence by producing more mucus and AMPs. Therefore,

in addition to basal production, we add a bacteria-dependent production term based on total bacteria density in the outer mucus compartment denoted by $f_B^O = \sum_{b\in\mathcal{B}} f_b^O$.

$$U_S^I[y] = \begin{cases} \frac{\Gamma^I}{V^I} v_m \hat{\rho_{gc}}(t) \bar{R}(f_B^O) - \frac{\Gamma^O}{V^I} v_m^{I,O}(t) y^I & \text{if } y = f_m, \\ \frac{\Gamma^I}{V^I} v_{AMPs} \hat{\rho_{ent}}(t) \bar{R}(f_B^O) - \frac{\Gamma^O}{V^I} v_{AMPs}^{I,O} y^I & \text{if } y = c_{AMPs}, \\ \frac{\Gamma^I}{V^I}\ v_{O_2}\ c_o^{top}(t) - \frac{\Gamma^O}{V^I}\ v_{O_2}^{I,O}\ y^I & \text{if } y = c_{O_2}, \\ 0 & \text{otherwise.} \end{cases} \tag{6}$$

Where $c_o^{top}(t)$ is the oxygen concentration at the top of the crypt given by the crypt model Eq. 22, $\hat{\rho_{ent}}(t) = N_{crypts} \times \rho_{ent}(t)$ and $\hat{\rho_{gc}}(t) = N_{crypts} \times \rho_{gc}(t)$ the total number of enterocyte and goblet cells in the colon section as we set N_{crypts} the total number of crypt in the section and $\rho_{ent}(t)$ and $\rho_{gc}(t)$ the total density of enterocyte and goblet cells in one crypt given by the crypt model Eq. 16. Here the the mucus flows $v_m^{I,O}(t)$ is time dependant and calculated to ensure constant volume.

We introduce $\bar{R}(f_B^O)$ as a linear additive function of basal production and bacteria presence induced production given by :

$$\bar{R}(f_B^O) = \theta + (1-\theta) R\left(f_B^O, K^{PPRs}, \kappa^{PPRs}\right) \tag{7}$$

with $R(.)$ being piece-wise activation function appreciated for its non asymptotic value in 0 and 1 given by Eq. 8. Parameters K^{PPRs}, κ^{PPRs} calibrate immune receptor sensitivity to bacterial presence in the outer mucus compartment and $0 \leq \theta \leq 1$ stands for basal production. As in [40] , function $R(.)$ takes the following form :

$$R(y, K, \kappa) := \begin{cases} 0 & \text{if } y \leq K - \kappa, \\ -\frac{1}{4\kappa^3} y^3 + \frac{3K}{4\kappa^3} y^2 - \frac{3K^2 - 3\kappa^2}{4\kappa^3} y + \frac{K^3 + 2\kappa^3 - 3K\kappa^2}{4\kappa^3} & \text{if } K - \kappa < y < K + \kappa, \\ 1 & \text{if } K + \kappa \leq y. \end{cases} \tag{8}$$

for $K > 0$ and $\kappa > 0$.

In the outer mucus compartment, mucus, AMPs and oxygen come from I and go to L :

$$U_S^O[y_i] = \begin{cases} \frac{\Gamma^O}{V^O}\ v_m^{I,O}(t)\ y_i^I - \frac{\Gamma^L}{V^O}\ v_i^{O,L}(t)\ y_i^O & \text{if } (y,i) = (f,m), \\ \frac{\Gamma^O}{V^O}\ v_i^{I,O}\ y_i^I - \frac{\Gamma^L}{V^O}\ v_i^{O,L}\ y_i^O & \text{if } (y,i) \in \{(c, AMPs), (c, O_2)\}, \\ 0 & \text{otherwise.} \end{cases} \tag{9}$$

Here $v_m^{O,L}(t)$ is also use to ensure constant compartment volume.

Concerning the lumen compartment, we emphasize mucus become liquid when it enters this compartment, representing the disassembly of the mucus

network. Then secretion flows are given by :

$$U_S^L[y_i] = \begin{cases} \frac{\Gamma^L}{V^L}\, v_i^{O,L}\, y_i^O & \text{if } (y,i) \in \{(c, AMPs), (c, O_2)\}, \\ 0 & \text{if } (y,i) = (f,m), \\ \frac{\Gamma^L}{V^L}\, v_m^{O,L}(t)\, f_m^O & \text{if } (y,i) = (f,l). \end{cases} \tag{10}$$

Absorption flows Standing in contrast to secretion flows are absorption flows. These are instigated by enterocytes located within the crypts. They apply to both metabolites and hydrogen sulfide (H_2S), which serve as energy sources for cells [31]. Absorption flows also apply to liquid l, playing a crucial role in food bolus solidification. We emphasize that as the wall is approached, the rate of absorption intensifies. This principle is applicable to the set $\mathcal{A} = \{(c, la), (c, ac), (c, pro), (c, but), (c, H_2S), (f, l)\}$.

$$U_A^x[y_i] = \begin{cases} -\frac{\Gamma^L}{V^L}\, v_i^{L,O}\, \hat{\rho_{ent}}(t)\, y_i^L & \text{if } x = L \text{ and } (y,i) \in \mathcal{A}, \\ \frac{\Gamma^L}{V^O}\, v_i^{L,O}\, \hat{\rho_{ent}}(t)\, y_i^L - \frac{\Gamma^O}{V^O}\, v_i^{O,I}\, \hat{\rho_{ent}}(t)\, y_i^O & \text{if } x = O \text{ and } (y,i) \in \mathcal{A}, \\ \frac{\Gamma^O}{V^I}\, v_i^{O,I}\, \hat{\rho_{ent}}(t)\, y_i^O - \frac{\Gamma^I}{V^I}\, v_i^{I,E}\, \hat{\rho_{ent}}(t)\, y_i^I & \text{if } x = I \text{ and } (y,i) \in \mathcal{A}, \\ 0 & \text{otherwise.} \end{cases} \tag{11}$$

Solute diffusion flows Some state variables, particularly gas and monosaccharide concentrations, do not experience absorption or secretion flows. We assume that they follow a passive motion in the environment with flow forms given by :

$$U_D^x[y_i] = \begin{cases} \frac{\Gamma^L}{V^L}\, v_i \left(y_i^O - y_i^L\right) & \text{if } x = L \text{ and } (y,i) \in \mathcal{G}, \\ \frac{\Gamma^L}{V^O}\, v_i \left(y_i^L - y_i^O\right) + \frac{\Gamma^O}{V^O}\, v_i \left(y_i^I - y_i^O\right) & \text{if } x = O \text{ and } (y,i) \in \mathcal{G}, \\ \frac{\Gamma^O}{V^I}\, v_i \left(y_i^O - y_i^I\right) & \text{if } x = I \text{ and } (y,i) \in \mathcal{G}, \\ 0 & \text{otherwise.} \end{cases} \tag{12}$$

with $\mathcal{G} = \{(c, mon), (c, CH_4), (c, CO_2), (c, H_2)\}$.

Bacterial active motion We include bacterial flows in our model as these organisms exhibit both active and passive movements. Passive movements are related to transit (Eq. 5) and mucus secretion, leading bacteria to follow the longitudinal flow and be vertically driven by mucus production with a shear coefficient b proportional to mucus flow $v_m^{O,L}(t)$. In the model, we highlight that all functional groups of bacteria are attracted to the mucus compartment with an adherence coefficient a, causing active movement of bacteria from the lumen compartment to the outer mucus compartment. Given that the inner mucus phase is generally bacteria-free or contains a limited number of adaptable bacteria in healthy cases, we model that functional groups cannot enter the inner mucus compartment.

$$U_M^x[y] = \begin{cases} \frac{\Gamma^L}{V^L} \left(b\, v_m^{O,L}(t)\, y^O - a\, y^L\right) & \text{if } x = L \text{ and } y \in (f_i)_{i\in\mathcal{B}}, \\ \frac{\Gamma^L}{V^O} \left(a\, y^L - b\, v_m^{O,L}(t)\, y^O\right) & \text{if } x = O \text{ and } y \in (f_i)_{i\in\mathcal{B}}, \\ 0 & \text{otherwise.} \end{cases} \tag{13}$$

Ensuring constant volumes In our modeling approach, we maintain constant volumes in compartments. Accordingly, we adjust $v^{out}(t)$ (transit flow on Γ^{out}), $v_m^{I,O}(t)$ (mucus flow between Γ^I and Γ^O), and $v_m^{O,L}(t)$ (mucus flow between Γ^O and Γ^L) at each time t. These adjustments are made in response to all volume fraction movements, adhering to the volume conservation principle:

$$\sum_{i\in\mathcal{V}} \dot{f}_i^x(t) = 0,\ x \in \mathcal{X}. \tag{14}$$

Therefore, they depend on all flows represented in the model. We also leverage the condition $\sum_{i\in\mathcal{V}} f_i^x = 1$ for these calculations, with detailed formulas provided in Appendix B.1. We should note that the transit slowdown is mimicked by ensuring $0 < v^{out}(t) < v^{in}$.

Inclusion of the metabolic and inflammatory response bacterial model. The inclusion of metabolic and inflammatory response bacterial model described in 2.1 is inspired from [20] adding our new component such as H_2S metabolisms representation. All processes are gathered in Table (1).

Table 1: **Processes notations**.

Processes	Notation
Mucopolysaccharide and Polysaccharide hydrolysis	P1
Protein and mucoproteine degradation and consumption	P2
Monosaccharide consumption	P3
Lactate consumption (oxidation and fermentation)	P4
Acetogenesis	P5
Methanogenesis	P6
H_2S toxicity on mucines	P7
Bacterial O_2 sensitivity	$P8, \phi$; $P8, \eta$
Bacterial death due to AMPs presence	P9
Bacterial natural death	P10
Gas transfer	P11

Metabolic reaction forms ($P1$-$P6$) Following [21] and [20], we model the kinetic rates of hydrolysis and protein degradation using the Contois equation [41], while the Monod equation [42] is employed to describe the kinetic rates for concentration utilization. Importantly, in the proposed model mucins

are represented as a volume fraction of mucus, which is the approach taken in [21, 20]. Mucins constitute approximately 5% of mucus, and we utilize this information when calculating our kinetic rates.

H_2S toxicity on mucins ($P7$) We model the degradation of mucins due to H_2S toxicity as a function of H_2S concentration, utilizing a constant rate formula: $k^{P7}R(c^x_{H_2S}, K^{P7}, \kappa^{P7}) \cdot 0.05 f^x_m$. In this equation, k^{P7} represents the maximal reaction rate, while $c^x_{H_2S}$ and f^x_m respectively denote the H_2S concentration and the mucus volume fraction within compartment $x \in \mathcal{X}$. Additionally, K^{P7} and κ^{P7} are tuning parameters applied to the function $R(.)$ function (Eq. 8).

Bacterial death ($P8$-$P10$) The model accounts for several bacterial death mechanisms, including natural death, sensitivity to inflammation (equivalent in our model to oxygen sensitivity), and control by AMPs. The rates of death induced by oxygen and AMPs are contingent on their respective concentrations in the given compartment. As with the process $P7$, reactions follow the form $k^p R(c^x_j, K^p, \kappa^p)$, with $(p, j) \in \{(P8, \phi; O_2); (P8, \eta; O_2); (P9, AMPs\}$. Furthermore, a constant rate of natural death, denoted as k^{P10}, is included for all bacterial groups.

Gases transfer ($P11$) In alignment with the methodology of [20], our model does not explicitly represent the gaseous phase. Instead, gas transfer from the dissolved to the gaseous phase is represented by the term $k^{P11}(c_j - K^{P11}_j RT[j, g]\infty)$ for $j \in G$. Here, $[j, g]\infty$ indicates the asymptotic value of the corresponding gas in the luminal portion as per [21]. An adjusted value for $[H_2S, g]\infty$ has been included, which was absent in the original model. R and T represent the ideal gas constant and temperature, respectively, while k^{P11} is the maximum specific rate and K^{P11}_j the Henry's Law coefficient [20].

Liquid management in processes In maintaining a constant volume, our model stipulates that the breakdown of the mixture phase, be it bacterial death or mucus degradation, liberates a corresponding volume of liquid. Similarly, we propose that bacterial growth is constrained by the available space in the liquid phase, and that an equivalent volume of liquid is utilized during the growth process.

Overall model reactions. We note P^x_f (resp. P^x_c) the Petersen reaction matrix for compartment $x \in \mathcal{X}$. P^x_f (resp. P^x_c) defines component yields in each of the processes included in the model (Table 1). For each compartment we also introduce kinetic rate vectors K^x_f and K^x_c and set $F^x = (F^x_i)_{i \in \mathcal{V}}$ and $C^x = (C^x_j)_{j \in \mathcal{D}}$ as:

$$F^x = P^x_f . K^x_f \quad \text{and} \quad C^x = P^x_c . K^x_c \quad \forall x \in \mathcal{X}. \tag{15}$$

F^x and C^x encompass all metabolic processes of polysaccharides and proteins degradation as well as bacterial death mechanisms and hydrogen sulfide toxicity on mucus bounds. Definitions of P_f^x, K_f^x, P_c^x and K_c^x are given in Annex in Tables (B.3) and (B.4).

2.2.2. Space-structured epithelial crypt model

The crypt model was originally proposed in [40] as a deterministic limit of a piecewise deterministic Markov process of birth and death structured in space and cell type. This model consists of two interacting parts: cell dynamics evolution within the crypt and solute diffusion (oxygen, SCFAs) as shown in the diagram Fig. 1. Unlike other parts of the multi-component model, this part representing the crypt maintains a one-dimensional spatial structure. This is achieved by projecting the crypt onto its vertical axis under symmetry assumption.

The model traces the evolution of distinct cell types: stem cells (sc), progenitor cells (pc), goblet cells (gc), and enterocytes (ent), all modelled as space-structured cell densities. Additionally, it includes the static cell density of deep crypt secretory cells (dcs). All variable are being stored in $\mathcal{C} = \{sc, dcs, pc, gc, ent\}$. These cells reside in the crypt and exert mechanical forces upon one another. For concentrations, the model represents oxygen's diffusion from the bottom of the crypt, originating from vessels beneath the epithelium, to the top, and conversely, the diffusion of butyrate produced by the microbiota from the top of the crypt to the bottom.

Model adaptations. First, we adapted the model to represent a human crypt as the original version was based on rodents. Second, we introduced Pattern Recognition Receptors (PPRs), already present in the colon flows model description. PPRs are innate immunity receptors present in or on cells that help to maintain symbiosis by acting on cell regulation processes, they impact stem and progenitor cell division. To account for this, in the model the division process is now stimulated by the volume fraction of bacteria in the outer mucus compartment that activate PRRs. We also included lactate, acetate and propionate diffusion along the crypt giving the set of metabolites $\mathcal{M} = \{la, ac, pro, but\}$. Furthermore, our model now includes an absorption term for metabolites, in addition to the β-oxidation term already defined in [40]. Lastly, we model a metabolic switch in differentiated cells, which is activated by the level of butyrate and inhibited by the level of hydrogen sulfide (H_2S) [43, 31].

In the following sections, we will briefly recall the existing model and present the working version of the crypt model, including these adaptations.

1D representation of the crypt geometry The crypt is modelled as a test tube shaped structure and projected on its vertical axis. Therefore, the densities and concentrations evolve along a segment $[0, Z_{max}]$ where Z_{max} is the top of the crypt.

Cell density migration and cell fate Cell migration is represented by a nonlinear degenerate parabolic equations. We denote $\rho_\ell(z,t)$ the density of cell type $\ell \in \mathcal{C}$ on $[0, Z_{max}]$, it undergoes a migration following $\forall \ell \in \mathcal{C} \setminus \{dcs\}$:

$$\begin{cases} \partial_t \rho_\ell - W \partial_z \left(\varphi(z) \rho_\ell \partial_z \rho\right) & = \sum_k \eta_{k,\ell} q_k Q_k(\ell, z, D\rho, \tilde{c}_{but}, f_B^O), \\ \rho_\ell(0,t) & = \rho_\ell^{bot}, \\ \partial_z \rho_\ell(Z_{max}, t) & = 0. \end{cases} \tag{16}$$

where $\rho(z,t) = \sum_{\ell \in \mathcal{C}} \rho_\ell(z,t)$ is the total local cell density. We refer the reader to [40] for the description of the coefficient $\varphi(z)$ accounting for curvature effect in the interactions between cells in the crypt and we recall its expression in Appendix B.3. Variable $\eta_{k,l}$ in the source term is given by :

$$\eta_{k,\ell} = \begin{cases} \rho_\ell & \text{if } k \in Div, \\ -\rho_\ell & \text{if } k \in Ex, \\ \rho_{\ell_k} & \text{if } k \in Dif \text{ and for a differentiation from type } \ell_k \text{ into type } \ell, \\ -\rho_\ell & \text{if } k \in Dif \text{ and for a differentiation from type } \ell. \end{cases} \tag{17}$$

where $Div = \{div, sc; div, pc\}$, $Ex = \{ex, gc; ex, ent\}$ and $Dif = \{sc, pc; pc, gc; pc, ent\}$ are respectively the set of division, extrusion and differentiation events. The maximal rate of cell fate event is given by the positive constant q_k and the function $Q_k(.)$ is linked to regulation mechanisms.

Cell fate event are regulated by different pathways listed in Table 2, where we added a new regulation by $PRRs$ compared to the original model. Functions Q_k are a combination of the activation function $R(y, K, \kappa)$ defined in Eq. 8, their detailed form are given in Appendix B.4.

Table 2: **Regulatory pathways for cell fate events.** This table enumerates different cell fate events and their respective regulatory pathways. Each event, denoted by k, is either negatively influenced ($-$), positively influenced ($+$), or unaffected ($\varnothing$) by pathway j.

		Regulation pathway (j)			
Cell fate event	Index (k)	Butyrate [but]	Wnt [z]	Density [$dens$]	PRRs [$prrs$]
Stem cell division	div, sc	$-$	$-$	$-$	$+$
Progenitor division	div, pc	$\varnothing$	$-$	$-$	$+$
Stem cell to progenitor diff.	sc, pc	$\varnothing$	$+$	$\varnothing$	$\varnothing$
Progenitor to goblet cell diff.	pc, gc	$+$	$+$	$\varnothing$	$\varnothing$
Progenitor to enterocyte diff.	pc, ent	$+$	$+$	$\varnothing$	$\varnothing$
Goblet cell extrusion	ex, gc	$\varnothing$	$+$	$+$	$\varnothing$
Enterocyte extrusion	ex, ent	$\varnothing$	$+$	$+$	$\varnothing$

Following [40], we assume that DCS cells are inactive, therefore their density remains constant in time. Although inactive, DCS cells exert a mechanical force on the cells surrounding them by their physical presence in the crypt influencing diffusion as part of the total density gradient $\partial_z \rho$ see Eq. (16). We use the same parametrized function to represent DCS cells density as in [40] which is recalled in Appendix B.5 and we use parameters adapted to human crypts given in C.6.

Metabolites and oxygen reaction-diffusion In the crypt, SCFAs generated by microbial metabolism diffuse until they are either absorbed or metabolized by the epithelium. Butyrate plays a crucial role in the host-microbiota symbiosis, as its presence is associated with the activation of β-oxidation, a metabolic process in epithelial cells consuming O_2 [12]. Within butyrate depleted environment cells switch from β-oxidation to anaerobic glycolysis, a oxygen-consumption free process [12]. This non-consumption of O_2 results in increased oxygen concentration in the lumen, negatively impacting oxygen sensitive commensal anaerobic bacteria group (indexed by ϕ and η in the functional microbiota representation). Consequently, fatty acid metabolism and symbiosis rely on butyrate presence. Moreover, we represent H_2S inhibition of β-oxidation when its luminal concentration reaches high levels [31, 44]. As we haven't introduced H_2S metabolism by differentiated cells [31] in the model so far, we excluded H_2S concentration from the crypt model, although its absorption rate is included in the colon flows model.

Oxygen, supplied by the blood vessels in the colon wall, diffuses into the crypt and is consumed by enterocytes and goblet cells during β-oxidation, which we summarise as follows:

$$
\begin{aligned}
\text{Lactate } (C_3H_6O_3): &\quad 2C_3H_6O_3 + 3O_2 \longrightarrow \text{energy and by-products} \\
\text{Acetate } (C_2H_3O_2): &\quad 2C_2H_3O_2 + 3O_2 \longrightarrow \text{energy and by-products} \\
\text{Propionate } (C_3H_6O_2): &\quad 2C_3H_6O_2 + 3O_2 \longrightarrow \text{energy and by-products} \\
\text{Butyrate } (C_4H_8O_2): &\quad 2C_4H_8O_2 + 7O_2 \longrightarrow \text{energy and by-products}
\end{aligned}
$$

Stoichiometric coefficient for butyrate metabolism were adapted compared to the original model. SCFAs are not only metabolized, but also absorbed by enterocytes, their concentrations being detected in the portal vein [45, 18]. Based on these reactions the concentrations of metabolites $\tilde{c_i}$(z,t) $i \in \mathcal{M}$ in the crypt evolve according to the following reaction/diffusion equation :

$$
\begin{cases}
\partial_t \tilde{c_i} - \sigma_i \partial_{zz} \tilde{c_i} &= -s_i \beta(\tilde{c_i}, \tilde{c_o}, \tilde{c_{but}}, c^L_{H_2S}(t), \rho_{gc}(z,t) + \rho_{ent}(z,t)) - \gamma_i^\alpha \rho_{ent}(z,t)\tilde{c_i}, \\
\tilde{c_i}(Z_{max}, t) &= c_i^I(t), \\
\partial_z \tilde{c_i}(0,t) &= 0.
\end{cases}
\tag{18}
$$

For each metabolite, the diffusion rate is denoted by σ_i, the absorption depends on enterocytes density ρ_{ent} and occurs at rate γ_i^α. The equivalent metabolite concentration obtained in the internal mucus compartment $c_i^I(t)$ is found in the Dirichlet boundary condition at the top of the crypt. β-oxidation is preceded by a stoichiometric soefficient s_i and is given by :

$$\beta(\tilde{c}_i, \tilde{c}_o, \tilde{c}_{but}, c^L_{H_2S}, \rho_{gc} + \rho_{ent}) = \gamma_i^\beta \frac{\tilde{c}_o^{s_{o,i}} \tilde{c}_i^{s_i}}{\tilde{c}_o^{s_{o,i}} \tilde{c}_i^{s_i} + K_i^{s_{o,i}+s_i}} (\rho_{gc} + \rho_{ent}) \tag{19}$$

$$\times R(\tilde{c}_{but}(z,t), K_{HIF}, \kappa_{HIF}) \tag{20}$$

$$\times (1 - R(c^L_{H_2S}(t), K_{H_2S}, \kappa_{H_2S})), \tag{21}$$

where $\tilde{c}_o$ is the oxygen concentration and $s_{o,i}$ is the stoichiometric coefficient of oxygen in the reaction. The maximum reaction rate is represented by γ_i^β, the affinity constant of β-oxidation is denoted by K_i, the density of differentiated cells in the crypt is calculated as $(\rho_{gc} + \rho_{ent})$. The regulatory pathways of β-oxidation are governed by the regulatory function $R(\tilde{c}_{but}, K_{HIF}, \kappa_{HIF})$ and $(1 - R(c^L_{H_2S}, K_{H_2S}, \kappa_{H_2S}))$ from Eq. 8. Additionally, $c^L_{H_2S}(t)$ is the concentration of H_2S in the lumen compartment of the colon model, we chose this compartment instead of the inner mucus one, closer, because [31] reports a toxic concentration measured in the lumen.

We recall that oxygen diffuses and is being consumed during cell metabolism process, giving the diffusion-reaction PDE :

$$\begin{cases} \partial_t \tilde{c}_o - \sigma_o \partial_{zz} \tilde{c}_o &= -\sum_{i \in \mathcal{M}} s_{o,i} \beta(\tilde{c}_i, \tilde{c}_o, \tilde{c}_{but}, c^L_{H_2S}, \rho_{gc} + \rho_{ent}), \\ \tilde{c}_o(0,t) &= \tilde{c}_o^{bot}, \\ \partial_z \tilde{c}_o(Z_{max}, t) &= 0. \end{cases} \tag{22}$$

3. Simulation process

3.1. Numerical schemes

The simulation employs a finite difference method to solve ODEs from the colon model part. In this scheme, we treat destruction terms implicitly and production terms explicitly to ensure numerical stability, positivity and efficiency. Furthermore, we solve the liquid fraction equation in the colon compartments by applying the fraction volume definition: $\sum_{i \in \mathcal{V}} f_i^x(t) = 1$. This enables us to bypass the need to directly solve for the liquid fraction by using $f_l^x(t) = 1 - \sum_{i \in \mathcal{V}, i \neq l} f_i^x(t)$.

As initial conditions, we use in the lumen compartment $f_i^L(0) = f_i^{in}\ \forall i \in \mathcal{M} \setminus \{l\}$, in the outer mucus we use $f_m^O(0) = 0.02$, $f_{pol}^O(0) = f_{prot}^O(0) = 0$ and $f_i^O(0) = f_i^{in}\ \forall i \in \mathcal{B}$ and in the inner mucus phase we set $f_m^I(0) = 1$. All concentrations in each compartment are set to zero.

Nonlinear degenerate parabolic equations Eq. 16 are not trivial to solve due to the non linear cross-diffusion terms and require adapted numerical tools. As in [40] we use the Explicit Kinetic Diffusive (EDK) scheme [46] designed for non linear transport diffusion equations to obtain satisfactory simulation results. Before using the numerical scheme, we had to transform equations into a conservative form given by :

$$\begin{cases} \partial_t \rho_\ell - \partial_z A(\rho_\ell, \rho, z) - \partial_{zz} B(\rho_\ell, z) & = \sum_k \eta_{k,\ell} q_k Q_k(\ell, z, D\rho, c_{but}, f_B^O), \\ \rho_\ell(0,t) & = \rho_\ell^{bot}, \\ \partial_z \rho_\ell(Z_{max}, t) & = 0. \end{cases} \tag{23}$$

with $A(\rho_\ell, \rho, z) = W\left(\varphi(z)\rho_\ell \partial_z(\rho - \rho_\ell) - \frac{1}{2}\varphi'(z)\rho_\ell^2\right)$ and $B(\rho_\ell, z) = \frac{W}{2}\varphi(z)\rho_\ell^2$. We adopt a splitting approach, where we first address the homogeneous equation, and subsequently solve the remaining EDO for the right hand side. Importantly, we distinguish between positive and negative source terms during this process by making the former explicit and the latter implicit in the resolution process

Concerning diffusion-reaction equations on concentrations we follow the same strategy as for cell density equations by splitting the resolution of the diffusion, solving it first and then solving the ODE related to the reaction part in the left hand side. Here we also pay attention to positive and negative source terms by letting the former explicit and the latter implicit in the resolution.

Simulations begin with zero concentrations in the crypt and a stationary state for cell densities. The stationary state of cell densities is obtained by isolating the crypt from the colon. This is done using symbiotic values for lactate, acetate, propionate, and butyrate at the crypt's top, H_2S concentrations in the lumen, and the bacterial fraction volume in the outer mucus. To obtain the initial densities for all $\ell \in \mathcal{C} \setminus \{dcs\}$ to:

$$\rho_\ell^0(z) = 0 \quad \forall z \in [0, Z_{max}].$$

The boundary conditions for the concentrations are defined as $\tilde{c}_{la}^{top} = 3.5mM$, $\tilde{c}_{ac}^{top} = 60mM$, $\tilde{c}_{pro}^{top} = 20mM$, and $\tilde{c}_{but}^{top} = 20mM$. The H_2S concentration and bacterial fraction volume in the lumen remain constant in time set to $c_{H_2S}^L = 0.1mM$ and $f_B^O = 0.015$. respectively.

For the actual coupling simulations, we avoid using an empty crypt initial state for three reasons: (i) this would be computationally very expensive, (ii) we want to reproduce realistic situations and we are not investigating crypt morphogenesis, and (iii) starting from empty crypts leads to aberrant behavior or errors since the absorption and secretion flows in the colon part of the model depend on differentiated cells.

3.2. Simulation strategies

To reconcile the differing scales of longitudinal and transverse flow in the colon and to better visualize the effects of changes, such as dietary alterations we propose to simulate a sequence of five colon sections. By employing a sectional approach, we provide a minimalist spatial representation that captures the essential dynamics while maintaining computational efficiency and manageability.

The simulation procedure unfolds sequentially. We start by setting the inputs for the first section, and the inputs for each subsequent section are then

determined by the concentrations and volume fractions obtained at the stationary state of the previous section. This methodology ensures a smooth transition between sections and maintains the model's consistency. To preserve volume constancy across sections, we adjust the input flow v^{in} for each section to match the output flow v^{out} of its preceding section at stationnary state. Therefore, the proposed strategy enables us to more effectively visualize the impact of various changes than a single section simulation, while remaining more manageable than a full 2D model.

While it is possible to conduct a simulation of all the sections in a stepwise temporal manner, such a procedure can significantly lengthen the simulation duration. However, our primary focus in this study is to understand the stationary states rather than the transition dynamics. Consequently, we opted not to employ this comprehensive temporal framework in our primary simulations, even though this approach is indeed feasible and is incorporated in the Python source code, available at **https://forgemia.inra.fr/marie.haghebaert/hostmicrobiota-interactions**. This decision helped us strike a balance between simulation accuracy, computational efficiency, and alignment with our objectives.

4. Simulation results

Simulations executed using the previously described model aim to effectively mimic a healthy human environment. This encompasses elements such as microbial diversity and density, colon physiology and crypt dynamics, under the influence of reference dietary fiber and protein intakes. We leverage the model's exploratory capacities to carry out a numerical experiment that illustrates the impact of diet on the model's equilibrium. This is achieved by studying the effects of variations in protein and fiber intake on bio-markers indicative of symbiosis, such as oxygen concentration in the lumen, PRRs activation rate or the ratio of $B^{\delta}_{H_2s}$ bacterial groups. Furthermore, we focus on a specific scenario involving an epithelial barrier breach, a condition that can potentially instigate dysbiosis. We examine the differential impacts under a reference healthy diet and a High Protein / Low Fiber (HP/LF) diet, which illuminates the model's capacity for dietary response and homeostasis maintenance. All the parameters used to run our simulation are collected in Appendix C.5 and C.6.

4.1. The reference healthy state

4.1.1. Microbial composition

In our model, we simulate the microbial distribution in the lumen as depicted in Fig. 7. This closely aligns with the results presented in [20] where monosaccharides degraders, represented as B^{ϕ}_{mon} and B^{μ}_{mon}, are the most prevalent groups ($\simeq 50\%$). They are followed by a smaller proportion of lactate consumers ($\simeq 26\%$), represented by the B^{ϕ}_{la}, B^{μ}_{la}, and B^{δ}_{la} groups. The hydrogenotrophic groups, $B^{\phi}_{H_2a}$ and $B^{\phi}_{H_2m}$, are even less prevalent, respectively $14,7\%$ and 1.8%. It's noteworthy that bacterial groups sensitive to inflammation (denoted as ϕ) are found in higher concentrations within the lumen. In contrast to the lumen, the outer mucus compartment primarily contains bacteria that are either tolerant to inflammation (denoted as μ) or are insensitive to it (denoted as δ). Given that our model utilizes oxygen concentration as an inflammation marker, this distribution aligns well with the anticipated behaviors of strict anaerobes and facultative anaerobes. Specifically, the presence of B^{δ}_{la} and $B^{\delta}_{H_2s}$ at 13.8% and 30.8% respectively, in this compartment facilitates a decrease in the oxygen concentration within the lumen, owing to their utilization of oxygen during oxidative metabolism. Coupled with β-oxidation, this process aids in maintaining the hypoxic environment of the lumen. Moreover, the modest concentration (0.1%) of $B^{\phi}_{H_2m}$ bacteria in the outer mucus compartment reflects the high oxygen sensitivity inherent to methanogens.

Our analysis reveals a greater bacterial volume fraction within the mucus ($f^O_B = 0.013$), compared to the lumen ($f^L_B = 0.006$). This difference is consistent with the result illustrated in Figure 4 of [20]. Moreover [20] projected the total bacterial volume fraction at the colon's exit to be approximately 0.06. Given the distal part of the colon is known to harbor a denser bacterial concentration than the transversal one, our results appear to be appropriately scaled.

The bacterial volume in the fifth section, in both the outer mucus and lumen compartments, computes to $f^O_B \times V^O + f^L_B \times V^L = 0.125cm^3$. To simplify, we

posit that all phases possess the same density as water, hence, $\rho_{f_i} = 1g/cm^3$ for each $i \in \mathcal{V}$. Therefore, we estimate the section to accommodate approximately $0.125g$ of bacteria, which is a reasonable amount for the transverse colon [20].

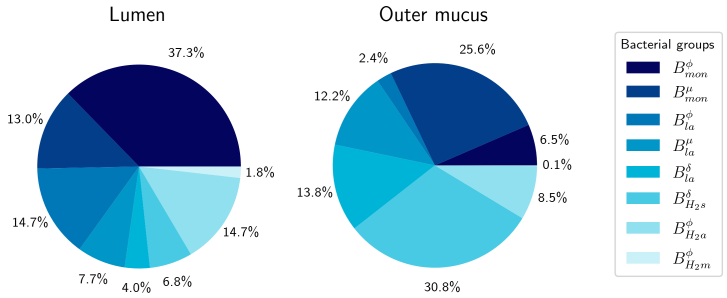

Figure 7: **Bacterial group proportions in Lumen and outer mucus layer**. We use plot pie to represent microbiota composition in the lumen and the outer mucus compartment of the model. Results are obtained at steady state for the last of the five sections analysed.

4.1.2. Colon physiology

Concerning longitudinal flows (Fig. 8a), proportionately scaled for this compact representation of the colon, the model faithfully captures the natural increase in bacteria count, reflecting the proliferation of the bacterial load when moving towards distal colon. The model also correctly depicts the decrease in transit flow, a feature associated with water absorption and stool formation.

In the simulation, we observe a subtle reduction in the total SCFA concentration along the section, as illustrated in figure (Fig. 8a). This aligns with the observed decrease in SCFA concentration throughout the colon [45]. However, the model predicts a concentration of $92.7mM$, which is somewhat lower than the biological measurements reported by [45]. Their study found that the concentration for six individuals averaged approximately $117 \pm 9mM$ in the transverse colon. Moreover, the ratio of SCFAs computed from the model simulation in the lumen for acetate, propionate, and butyrate are 54:23:23, which is close to that observed in [45] worth 57:21:22 in the descending colon.

Turning our attention to the transverse gradients (Fig. 8b), the model successfully generates a hypoxic environment in the lumen, mirroring the natural low-oxygen conditions typical in the colon. This reinforces the model's accuracy in simulating the colon's physiological state. In the inner mucus layer, the simulation generates higher concentrations of AMPs compared to the outer mucus layer and the lumen compartments, underlining the protective role of the mucus in preventing bacterial invasion.

H_2S concentration decreases from the lumen compartment to the inner mucus one and remains in healthy concentration level $< 1mM$[31].

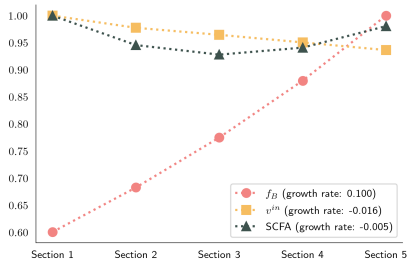

(a) Evolution along 5 sections.

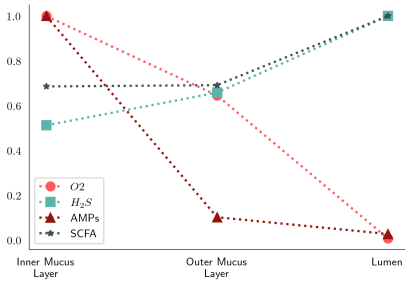

(b) Gradients from lumen to the inner mucus layer in section 5.

Figure 8: **Longitudinal and transverse gradients in colon physiology**. a) Evolution of total bacterial fraction volume, total SCFAs concentration and transit flows in the lumen compartment along 5 sections. Depicted values are divided by their maximum, for SCFAs : $94.5mM$, for transit v^{in} : $0.416cm.h^{-1}$ and for bacterial fraction volume : $6.1e-3$[.]. b) Concentration gradient from lumen to the inner mucus layer for oxygen, H_2S, antimicrobial peptides (AMPs) and SCFAs. Values are divided by their max, for SCFAs : $92.7mM$, for H_2S : $0.2mM$, for AMPs : $0.47mM$ and for oxygen $6.7[a.u]$.

4.1.3. Epithelial crypt dynamic

Epithelial cells. In our simulation (Fig. 9), the total cell count per crypt is 2231, closely aligning with the literature value of 2427.8 ± 504.4 from [47]. Our model yields 603 proliferative cells, encompassing both stem and progenitor cells, compared to 623.9 ± 234.1 and 1592 differentiated cells versus 1768.2 ± 434.5 in the cited source. Moreover, the model appropriately replicated the stem cell niche, the proliferative zone, and the differentiated zone. The ratio of goblet cells to enterocytes was observed to be one-third, aligning well with the expected distribution [40].

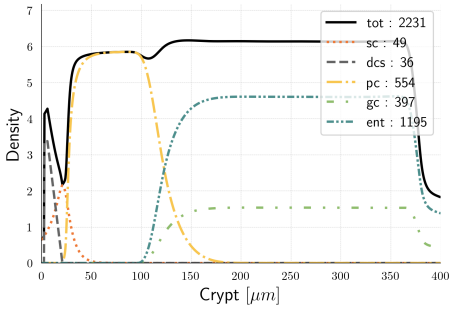

Figure 9: **Cell densities along the crypt**. Cell densities are plotted as a function of the height in the crypt. The total number of cells is reported in the box for each cell type.

Metabolites and oxygen. Upon comparison of our simulation results with the existing literature (see fig 10), we found a good agreement. For instance, our simulated oxygen gradient from the bottom to the top of the crypt was 7.35.

This value is in the same order of magnitude as the results presented in figure 1A from [11], which depicts the oxygen partial pressure gradient between host tissues and the lumen in a healthy situation.

Our simulations suggest that at the crypt base SCFAs ratios are 66:21:12. This is in close agreement with the literature-reported ratio of 71:21:8 observed in the portal vein [45]. Specifically, our model yielded concentrations of $0.83, mM$ for butyrate which corresponds with the upper limit of the reported range of $0.05 - 0.8, mM$ [18]. Using the butyrate concentration and the portal vein ratio, we calculated the concentrations of acetate and propionate at the crypt base to fall between $0.44 - 7.10 mM$ and $0.13 - 2.1 mM$, respectively. These calculations align closely with our experimental results, which showed concentrations of $4.46 mM$ for acetate and $1.42 mM$ for propionate.

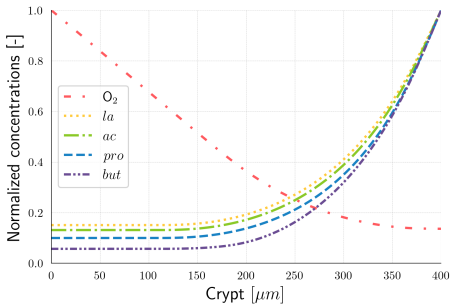

Figure 10: **Normalized solutes concentration along the crypt**. Concentration are divided by their maximum values, for oxygen : $48.8[a.u]$, for lactate : $0.48 mM$, for acetate : $34.05 mM$, for propionate : $14.30 mM$ and for butyrate : $14.72 mM$.

4.2. Numerical exploration to assess diet effect

Building on the validity of our model in reproducing a healthy state, our next objective is to explore its behavior in response to dietary variations. This aspect of our research is motivated by two primary goals: firstly, to elucidate the effects of fiber and protein inputs on symbiosis' biomarkers, and secondly, to evaluate the model's capacity to capture the responses to a high protein diet.

4.2.1. Numerical framework

Our experimental design draws from the study of Russel et al. [9], which investigated weight-loss diets and provided experimental results for protein and fiber intakes across three diet types: (i) a reference diet with standard protein and fiber intakes, (ii) a high-protein/high-fiber diet, and (iii) a high-protein/low-fiber diet. Using data from this research, we derived a realistic range for protein and fiber fraction volume intakes, specifically focusing on the transverse colon to perform an *in silico* experiment.

The volume fraction of polysaccharides introduced at the lumen input surface, Γ^{in}, of the initial section is set to lie between 0.02 and 0.06. Depending

on this value, we adjust the concentrations of various substances: monosaccharide, lactate, acetate, propionate, and butyrate, proportionally. Drawing from the values in [9], the concentration ranges are set as follows: $[1 \times 10^{-}5, 4 \times 10^{-}5]mM$ for monosaccharide, $[2.5 \times 10^{-}6, 5.5 \times 10^{-}6]mM$ for lactate, $[3 \times 10^{-}5, 7 \times 10^{-}5]mM$ for acetate, $[1 \times 10^{-}5, 2.5 \times 10^{-}5]mM$ for propionate, and $[5 \times 10^{-}6, 2.5 \times 10^{-}5]mM$ for butyrate. The protein volume fraction spans from 0.01 to 0.03.

To visualize the data, we employed an 8×8 grid in the protein/fiber space and utilized interpolation for heatmap generation. For each parameter space point, we calculated the model across five sections, adjusting the dietary input in primary section. We then emphasized the steady-state results observed in the 5th section, with each section computed sequentially until $T_{max} = 400h$.

In our numerical analysis, we prioritize four essential biomarkers serving as indicators of symbiosis :

1. Oxygen concentration in the lumen compartment c_o^L: an elevated oxygen level promotes a dysbiotic state, fostering facultative anaerobes and inflammation-resistant bacteria.
2. The ratio of $B_{H_2s}^{\delta}$ volume fraction to the total bacterial volume fraction in the lumen compartment: an increased proportion of this facultative, inflammation resistant bacterial group can be seen as a dysbiotic environment.
3. Function $\bar{R}(f_B^O)$, as detailed in Eq. 7, represents a surrogate for PRRs activation. This marker correlates with the production of AMPs and mucus, vital for sustaining the epithelial barrier.
4. The aggregate count of differentiated cells in the crypt, denoting crypt maturity: crucial to maintain the colon's healthy functionality in absorption and secretion and ensure an hypoxic lumen environnement.

4.2.2. Impact of diet on symbiosis biomarkers

Oxygen concentration in the lumen. The concentration of oxygen in the lumen is primarily influenced by dietary fiber input (Fig. 11). Above a threshold, the oxygen concentration in the lumen approaches 0. However, for low fiber input, the oxygen concentration increases, mainly due to the reduced production of butyrate. This, in turn, leads to a lower number of differentiated cell and a potential shift in epithelial cell metabolism, which leaves oxygen coming from vessels beneath the epithelium unconsumed.

$B_{H_2s}^{\delta}$ group proportion in the lumen. Our model uncovers a correlation with protein intake, suggesting that a high protein diet could foster the growth and predominance of this bacterial group (Fig. 12a).

However, an intriguing observation is the mitigating effect of a high-fiber diet against the negative impacts of high protein intake. The model illustrates a negative correlation between fiber intake and the proportion of $B_{H_2s}^{\delta}$ group, underscoring dietary fibers' role in nurturing a diverse and balanced gut microbiota. This simulation result suggests that a diet rich in fibers could potentially offset the dysbiosis induced by a protein-dense diet, echoing findings from [9].

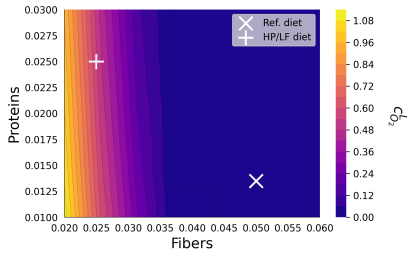

Figure 11: **Oxygen concentration in lumen influenced by diet.** This impact is displayed when varying fiber and protein intake on a grid $[0.02, 0.06] \times [0.01, 0.03]$ as a function of fiber and protein supply.

A less intense but significant correlation is also detected between the total dietary intake volume and these bacteria's proportions, with a decline in facultative anaerobes observed as total intake decreases (Fig. 12b).

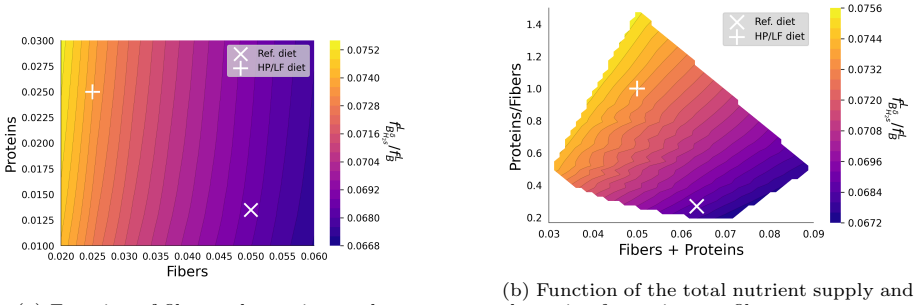

(a) Function of fiber and protein supply.

(b) Function of the total nutrient supply and the ratio of protein over fiber.

Figure 12: **Ratio of $B^{\delta}_{H_2 s}$ fraction volume to total bacterial fraction volume in the lumen influenced by diet.** This impact is displayed when varying fiber and protein intake on a grid $[0.02, 0.06] \times [0.01, 0.03]$.

Pattern Recognition Receptors (PRRs) activation. Our model highlights a positive correlation between PRRs activation and the total volume of dietary intake (Fig. 13b). Primarily, this relationship is driven by the decrease in bacterial volume when the diet lacks sufficient fiber and protein content, leading to a simplified carbohydrate degradation trophic chain.

Moreover, we identified a significant secondary correlation between PRRs activation and protein intake (Fig. 13a). The facultative anaerobes bacteria, specifically the $B^{\delta}_{H_2 s}$ group, thrive in protein-rich environments and demonstrate increased division and proliferation rates due to their oxidative metabolism which results in a higher bacterial fraction volume in the mucus compartment.

Differentiated cells density within the crypt. Dietary intake demonstrably influences crypt maturity (Fig. 14). A highlight from our study is the positive correlation between crypt maturation and fiber intake. This correlation can be

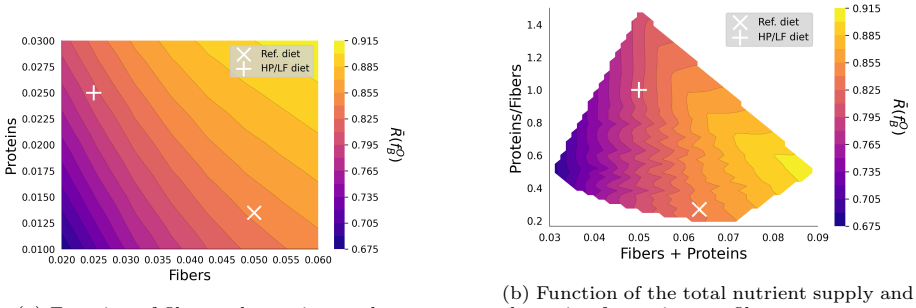

(a) Function of fiber and protein supply.

(b) Function of the total nutrient supply and the ratio of protein over fiber.

Figure 13: **Pattern Recognition Receptors (PRRs) activation influenced by diet.** Visualization of the effect of varying fiber and protein supply on PPR activation. This impact is displayed when varying fiber and protein intake on a grid $[0.02, 0.06] \times [0.01, 0.03]$.

attributed to the role of butyrate in promoting cell differentiation, emphasizing the significance of dietary fiber in the process of crypt maturation. On the other hand, our simulations suggest that protein intake does not have a pronounced impact on crypt maturity in our model.

For a more detailed insight into the effects of protein and fiber on crypts, refer to section 5 in Fig. 18a and Fig. 18c, which illustrate cell distributions under reference and HP/LF diets. The latter one results in comparatively immature crypts, characterized by fewer differentiated cells (1514 vs. 2190) and more proliferative cells (678 vs. 610). Although the numerical differences might appear subtle, the qualitative observations indicate a trend towards crypt immaturity with reduced fiber intake.

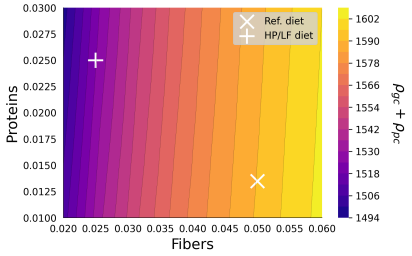

Figure 14: **Total number of differenciated cells in one crypt influenced by diet**. This number is displayed when varying fiber and protein intake on a grid $[0.02, 0.06] \times [0.01, 0.03]$ as a function of fiber and protein supply.

4.3. Symbiosis resilience when facing inflammation episodes

This section is dedicated to showcasing the model's ability to switch equilibria, evaluate the diet's impact on health recovery, and simulate situations critical to the host-microbiota symbiosis.

4.3.1. Modeling a breach in the epithelial barrier

In this exploration, we replicate a disruption in the epithelial barrier, indicated by an oxygen bloom at the crypt's bottom ($\tilde{c_o}^{bot,breach} = 1.5 \times \tilde{c_o}^{bot}$), and a surge in AMPs secretion ($v_{AMPs}^{breach} = 1.5 \times v_{AMPs}$), symbolizing a deterioration in mucus quality and the corresponding immune system compensation. This disturbance is locally incorporated into colon sections 2, 3, and 4.

4.3.2. Assess the impact of two different diets

To scrutinize the diet's impact on the resilience of symbiosis, we contrast the state in section 5 under two distinct dietary regimes: the Reference healthy diet with high fiber and normal protein intake, and a HP/LF diet, both highlighted in Fig. 11, Fig. 12, Fig. 13, Fig. 14.

The HP/LF diet is modeled with a volume fraction of fiber entering the first section $f_{pol}^{in} = 0.025$ and a protein fraction volume entering $f_{prot}^{in} = 0.025$. For this diet, we adjusted SCFAs inputs to $c_{mon}^{in} = 1.25 \times 10^{-5} mM$, $c_{la}^{in} = 3.125 \times 10^{-6} mM$, $c_{ac}^{in} = 3.75 \times 10^{-5} mM$, $c_{pro}^{in} = 1.25 \times 10^{-5} mM$, and $c_{but}^{in} = 6.25 \times 10^{-6} mM$.

The Reference diet is the one used to simulate the healthy reference state (See 4.1), featuring a volume fraction of fiber entering the first section $f_{pol}^{in} = 0.05$ and an entering protein fraction volume $f_{prot}^{in} = 0.0135$. For this diet, SCFAs inputs are $c_{mon}^{in} = 3.33 \times 10^{-5} mM$, $c_{la}^{in} = 3 \times 10^{-6} mM$, $c_{ac}^{in} = 6 \times 10^{-5} mM$, $c_{pro}^{in} = 2 \times 10^{-5} mM$, and $c_{but}^{in} = 2 \times 10^{-5} mM$.

This comparison enables us to evaluate how dietary habits, specifically the equilibrium between protein and fiber, can influence the resilience of host-microbiota symbiosis under stress conditions.

To carry out our investigation, we adopt a systematic approach to examine the effects of disturbances on our model. Initially, we exclusively explore the influence of the oxygen bloom (scenario A). Next, our attention shifts to the increase in AMPs production rate (scenario B). Ultimately, we combine both influences for a holistic study in scenario C. For each scenario, considering their biological implications, we monitor the same outputs as the previous study : the oxygen level and the proportion of $B_{H_2s}^{\delta}$ in the lumen, and the mucus production rate, which depends on the density of differentiated cells and the activation of PRRs (Eq. 6). Specifically, for scenario C, we also evaluate the breach's effect on cell densities.

4.3.3. Scenario's results

Scenario A: Oxygen bloom at the crypt base. In this scenario, we simulate an oxygen bloom at the base of the crypts, serving as a proxy for a breach in the epithelial barrier. As expected, in both diets, the disturbance leads to a direct increase in the oxygen concentration in the lumen, with a more exacerbate effect observed under the HP/LF dietary regime (Fig. 15a).

This breach scenario also impacts the population of $B_{H_2s}^{\delta}$ bacteria. While no significant impact is noted up to section 2, a noticeable increase in the ratio of $B_{H_2s}^{\delta}$ is observed beyond this point under the HP/LF diet (Fig. 15b). At

this juncture, the oxygen concentration crosses the threshold that facilitates the growth of facultative anaerobes bacteria, leading to a higher density of $B^{\delta}_{H_2s}$ in the lumen post-breach.

Mucus production rate also varies under this scenario. A typical protective response of increased mucus production is observed under the reference diet. Conversely, under the HP/LF diet, mucus production is lower in the event of an oxygen breach, suggesting reduced defensive capabilities when a dysbiotic state is compounded by a low-fiber diet (Fig. 15c).

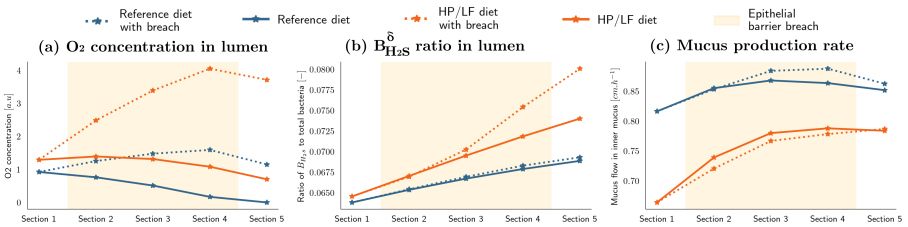

Figure 15: **Scenario A: effects of an oxygen bloom at the crypt base.** This figure represents the impact of an oxygen bloom at the crypt base, serving as a proxy for an epithelial barrier breach, under two different dietary regimes (Reference and HP/LF diets).

Scenario B: Increased AMPs Production. The second scenario involves an increase in AMPs production, representative of another potential breach in the epithelial barrier where mucus quality would be reduced and the innate immunity reacts by increasing AMPs production. This escalation does not significantly affect the oxygen concentration in the lumen but does contribute to a slight increase under the HP/LF diet regime (Fig. 16a).

Interestingly, one might have anticipated a higher ratio of $B^{\delta}_{H_2s}$ in the scenario with disturbance. However, our observations reveal the opposite, even if the disparity is minimal in both regime. This counter intuitive outcome further underscores the complex interplay within the system. This decline can be traced back to $B^{\delta}_{H_2s}$ reduced presence in the outer mucus compartment, attributed to diminished mucoproteins. This effect in the outer mucus compartment then impacts the lumen due to the movement of bacteria between these compartments (Fig. 16b).

With respect to mucus production, the rise in AMPs production leads to a decrease, consistent with the reduction in the number of bacteria necessary for activating PRRs in the mucus-producing goblet cells (Fig. 16c).

Scenario C: Combined Oxygen Bloom and Increased AMPs Production. The final scenario combines the impacts of both an oxygen bloom at the crypt base and increased AMPs production. Oxygen levels in the lumen mirror the patterns observed in scenario A, with a greater increase observed under the HP/LF diet (Fig. 17a).

The behavior of B_{H_2s} bacteria in this scenario is twofold: Up to section 2, we observe effects related to increased AMPs production with a slight decrease

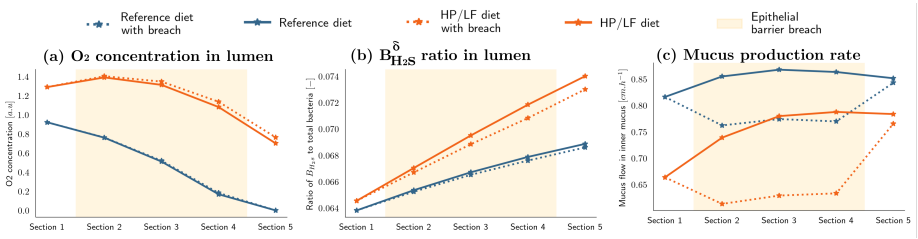

Figure 16: **Scenario B: effects of increased AMPs secretion.** This figure showcases the effects of a surge in AMPs secretion, simulating a reduction in mucus quality, under two different dietary regimes (Reference and HP/LF diets).

in the ratio. Then, from section 3 onwards, we notice a surge in B_{H_2S} bacteria, akin to the observations in the oxygen-only breach scenario (Fig. 17b).

Finally, in terms of mucus production, the responses mirror those found in scenario B, where a higher AMPs production leads to a decrease in mucus production (Fig. 17c).

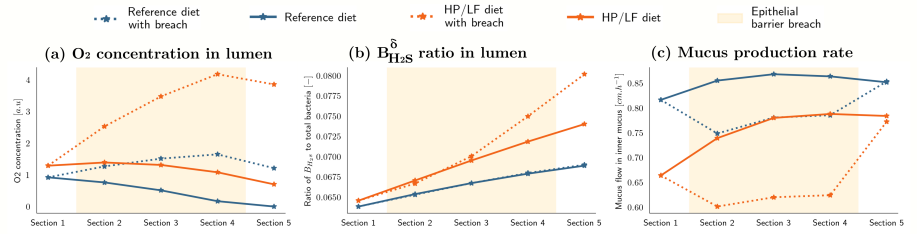

Figure 17: **Scenario C: combined effects of an oxygen bloom and increased AMPs secretion.** This figure demonstrates the combined impact of an oxygen bloom at the crypt base and an increased AMPs secretion, under two different dietary regimes (Reference and HP/LF diets).

Effect on the crypt cell densities. In our study, we analyzed diet and breach (specifically scenario C) effect on cell densities, as presented in Fig. 18. One observation is the effect of diet on the crypt's maturity. With the HP/LF diet, we identify an immature crypt profile characterized by a higher number of proliferative and a higher height in the crypt combined with a lower number of differentiated cells. This implies that the HP/LF diet qualitatively encourages formation of immature crypts in our context.

Moreover our simulation indicates a tendency of cell crypts under HP/LF diet to use self-regulation to revert to a healthy state (Fig. 18c). This is evidenced by the progressive modulation of cell densities across sections; from section 1 to section 5, there's a decline in the number and prominence of proliferative cells within the crypt (from 852 in section 1 to 678 in section 5). Concurrently, the count of differentiated cells increase, moving from 1322 in section 1 to 1514 in section 5.

While the dietary impact appears to be more pronounced on cell densities, the epithelial breach also plays a role across both diet types. Specifically, breaches visually amplify the presence of proliferative cells to the detriment of differentiated ones (Fig. 18b) and seems to delay the recuperative behavior in the HP/LF diet (Fig. 18d).

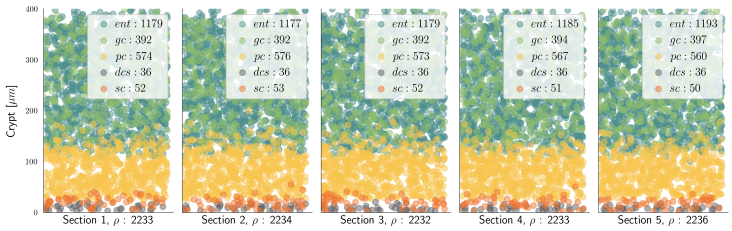

(a) Reference diet

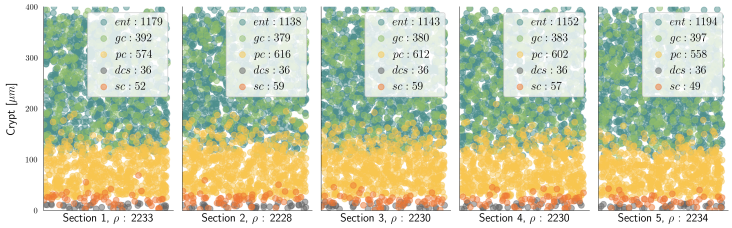

(b) Reference diet with breach

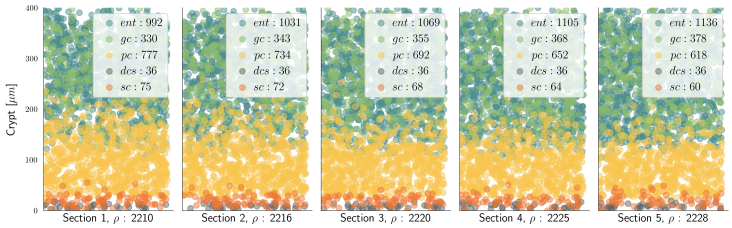

(c) HP/LF diet

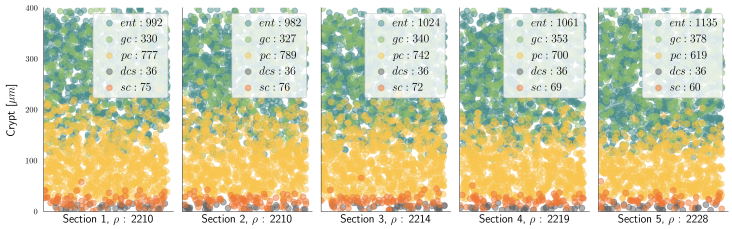

(d) HP/LF diet with breach

Figure 18: **Spatial distribution of cells in crypts under varying diet and breach scenario C.** The distribution is visualized in colon sections under different conditions: (a) Reference diet, (b) Reference diet with an epithelial breach, (c) HP/LF diet, and (d) HP/LF diet with an epithelial breach. In each depiction, cells are represented by circles, with their colors indicating distinct cell types. The distribution patterns are based on cell densities derived from the model.

5. Conclusive discussions

This research employed a comprehensive simulation model to explore the nuanced interactions between host and microbiota within the colon. Through our model, we discerned the implications of dietary variations, especially in the face of disturbances like epithelial breaches.

To build our model, we started from previous works of [21, 20, 25]. Our simulation, working at the scale of a colon section, depicted epithelial crypt dynamics influenced by the colonic environment. This environment is shaped by bacterial groups categorized by their metabolic capabilities. Drawing inspiration from data analysis, we introduced a bacterial group distribution correlating metabolism with inflammation sensitivity. By modeling innate immunity mechanisms at the epithelial scale, our representation of host-microbiota interactions is enriched.

We have also introduced new metabolic pathways such as protein degradation (already present in other model as [30]) leading to H_2S production. To do so, we introduced new bacterial flora representing sulfate reducing bacteria and those involved in cystein catabolism [31]. On top of that, by the inclusion of oxygen diffusion we are able to propose a new interaction mechanism focusing on bacterial tolerance of oxygen in the environment proposing a new interaction involved in the onset of dysbiotic equilibrium. To our knowledge, our model is pioneering in concurrently representing the epithelium dynamic, mucus production, diet intake, colon functions (transit, absorption), innate immune system at the epithelial scale, oxygen concentration and microbiota with bacterial mobility, metabolism and sensitivity to inflammation.

Our results emphasize the intricate nature of the host-microbiota relationship, spotlighting its vulnerability to dietary changes, especially diets high in protein but low in fiber. Simulations underscored the positive influence of total nutrient intake on innate immunity receptors in epithelial cells and the impact of protein/fiber ratios on facultative anaerobic bacterial groups. We also observed that fiber intake promotes crypt maturity, vital for the colon's absorption role, leading to a hypoxic environment via differentiated cell oxygen consumption.

Our findings accentuate the effects of diet on gut health, especially when confronted with challenges like epithelial breaches. HP/LF diet amplifies these challenges, fostering conditions conducive to dysbiosis, encouraging facultative bacteria proliferation, escalating inflammation, and pushing the microbiota towards a dysbiotic state. Notably, HP/LF diet seems to hinder mucus production, a crucial response to disturbances and vital for modulating host-microbiota interactions, suggesting diminished gut resilience under such diets.

While our model offers substantial insights, it also identifies areas for enhancement. For example, widening the protein degradation pathway by including intermediate metabolites as succinate like [30] and additional bacteria capable of degrading both fibers and proteins could offer deeper insights. In this context the model could also be connected to alternative representation of bacterial metabolism focusing on emblematic bacterial genera or species. Examples are the model design proposed in [48] or the use of genome scale metabolic

models, *e.g.* in [24]. The latter would, however, imply a higher computational cost. Periodicity in diet supply and oxygen concentration, variable mucus layer thickness considerations could also provide more holistic views.

In its current form, the model has a fixed input on Γ^{in} which restricts our analysis to transitory disturbance within the sections. To address this situation, future iterations of the model could integrate the 2D colon model from [20].

We acknowledge the model focuses on the epithelial cells' innate immunity. Including more information on the role of DCS cells in the crypt and a lamina propia or a blood compartment with the presence of immune cells could be a more sophisticated depiction of immune system. Moreover, introducing a bacterial virulence index might offer insights into targeted immune reactions.

In conclusion, this study represents a step forward in understanding the host-microbiota symbiosis within the colon. It shows the complex interplay between diet, health, and the gut's microbial environment. Despite areas for potential improvement, the current model provides critical insights into factors like oxygen concentration, protein degradation, primary immunity mechanisms, and the overall coupling effects within the colon ecosystem. Thus, our work lays a solid foundation for future exploration, investigation, and refinement, deepening our understanding of the intricate dynamics of host-microbiota symbiosis and the influence of diet.

Appendix A. Inflammatory response patterns among bacterial clusters

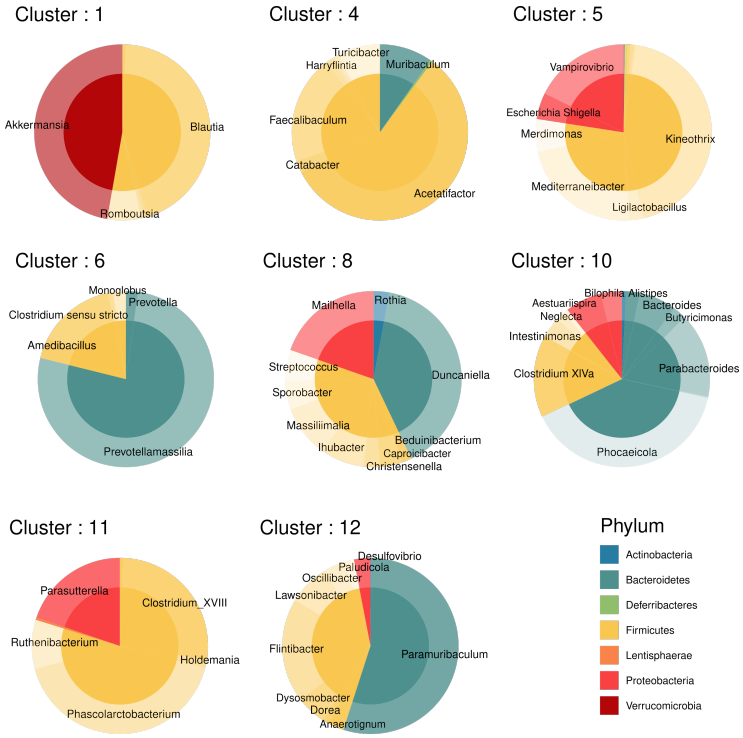

Figure A.19: **Cluster compositions from temporal analysis in rats with DSS-induced inflammation**. For each cluster presented in fig 3 the corresponding composition in term of genera is depicted in the figure. Here, for each cluster is represented the mean proportion of genera we do not explicitly show those with small proportions.

Appendix B. Model complements

Appendix B.1. Insuring compartments constant volumes

Unknown to identify : $v^{out}(t)$, $v_m^{I,O}(t)$, and $v_m^{O,L}(t)$ at each time. By summing fraction volume equations (2) for every compartment $x \in \mathcal{X}$ we need to satisfy a sum equal to 0. By definition we have $F_i^x = 0$ for each $i \in \mathcal{V}$. We set $f_B^x = \sum_{b \in B} f_b^x$. At time t, we should solve the system :

$$\left\{\begin{array}{ll} 0 & = \Gamma^{in}\left(v^{in} - v^{out}(t)(f_{pol}^L + f_r^L + f_l^L)\right) - \frac{V^L}{\tau + V^L/(\Gamma^{in} v^{out}(t))} f_{B_{bact}}^L \\ & \quad + \Gamma^L(b v_m^{O,L}(t) f_B^O - a f_B^L) - \Gamma^L v_l^{L,O} \hat{\rho_{ent}}(t) f_l^L + \Gamma^L v_m^{O,L}(t) f_m^O, \\ 0 & = \Gamma^O v_m^{I,O}(t) f_m^I - \Gamma^L v_m^{O,L}(t) f_m^O + \Gamma^L(a f_B^L - b v_m^{O,L}(t) f_B^O) \\ & \quad + \Gamma^L v_l^{L,O} \hat{\rho_{ent}}(t) f_l^L - \Gamma^O v_l^{O,I} \hat{\rho_{ent}}(t) f_l^O, \\ 0 & = \Gamma^I v_m \hat{\rho_{gc}}(t) \bar{R}(f_B^O) - \Gamma^O v_m^{I,O}(t) f_m^I + \Gamma^O v_l^{O,I} \hat{\rho_{ent}}(t) f_l^O - \Gamma^I v_l \hat{\rho_{ent}}(t) f_l^I. \end{array}\right. \tag{B.1}$$

This leads to the following result :

$$\left\{\begin{array}{ll} v_m^{O,L}(t) & = \frac{\Gamma^L a f_{B_{bact}}^L + \Gamma^L v_l^{L,O} \hat{\rho_{ent}}(t) f_l^L + \Gamma^I v_m \hat{\rho_{gc}}(t) \bar{R}(f_B^O) - \Gamma^I v_l \hat{\rho_{ent}}(t) f_l^I}{\Gamma^L(f_m^O + b f_{B_{bact}}^O)} \\ v_m^{I,O}(t) & = \frac{\Gamma^I v_m \hat{\rho_{gc}}(t) \bar{R}(f_B^O) + \Gamma^O v_l^{O,I} \hat{\rho_{ent}}(t) f_l^O - \Gamma^I v_l \hat{\rho_{ent}}(t) f_l^I}{\Gamma^O f_m^I} \end{array}\right. \tag{B.2}$$

Then, $v^{out}(t)$ is deduced from (B.1) using (B.2). The equation to solve got 2 roots. We choose the positive one as v^{out} should satisfy $0 < v^{out}(t) < v^{in}$.

Appendix B.2. Metabolic processes reaction terms

Table B.3: Peterson matrix $(P_f)^t$ and kinetic rate vector K_f.

	m	pol	$prot$	r	B^{ϕ}_{mon}	B^{η}_{mon}	B^{ϕ}_{la}	B^{η}_{la}	B^{δ}_{la}	$B^{\delta}_{H_2s}$	$B^{\phi}_{H_2a}$	$B^{\phi}_{H_2m}$	l	Kinetic K_f
$P1^{\phi}_{m}$	$-Y^{P1}_{m}$												Y^{P1}_{m}	$k^{P1}\frac{0.05\times f_m f_{B^{\phi}_{mon}}}{K^{P1}_f f_{B^{\phi}_{mon}}}\frac{K^{P1}_f}{+0.05\times f_m}$
$P1^{\eta}_{m}$	$-Y^{P1}_{m}$												Y^{P1}_{m}	$k^{P1}\frac{0.05\times f_m f_{B^{\eta}_{mon}}}{K^{P1}_f f_{B^{\eta}_{mon}}}\frac{K^{P1}_f}{+0.05\times f_m}$
$P1^{\phi}_{pol}$		$-Y^{P1}_{pol}$											Y^{P1}_{pol}	$k^{P1}\frac{0.05\times f_m f_{B^{\phi}_{mon}}}{K^{P1}_f f_{B^{\phi}_{mon}}}\frac{K^{P1}_f}{+0.05\times f_m}$
$P1^{\eta}_{pol}$		$-Y^{P1}_{pol}$											Y^{P1}_{pol}	$k^{P1}\frac{0.05\times f_m f_{B^{\eta}_{mon}}}{K^{P1}_f f_{B^{\eta}_{mon}}}\frac{K^{P1}_f}{+0.05\times f_m}$
$P2_{m}$	$-Y^{P2}_{m}$									$Y^{P2m}_{B_{H_2s}}$			$Y^{P2}_{m}-Y^{P2m}_{B_{H_2s}}$	$k^{P2_m} f_l \frac{0.05\times f_m f_{B^{\delta}_{H_{2s}}}}{K^{P2}_f f_{B^{\delta}_{H_{2s}}}}\frac{}{+0.05\times f_m}$
$P2_{prot}$			$-Y^{P2}_{prot}$							$Y^{P2_{prot}}_{B_{H_2s}}$			$Y^{P2}_{prot}-Y^{P2_{prot}}_{B_{H_2s}}$	$k^{P2_{prot}} f_l \frac{f_{prot} f_{B^{\delta}_{H_{2s}}}}{K^{P2}_f f_{B^{\delta}_{H_{2s}}}}\frac{}{+f_{prot}}$
$P3^{\phi}$					$Y^{P3}_{B_{mon}}$								$-Y^{P3}_{B_{mon}}$	$k^{P3} f_l \frac{c_{mon} f_{B^{\phi}_{mon}}}{K^{P3}_s + c_{mon}}$
$P3^{\eta}$						$Y^{P3}_{B_{mon}}$							$-Y^{P3}_{B_{mon}}$	$k^{P3} f_l \frac{c_{mon} f_{B^{\eta}_{mon}}}{K^{P3}_s + c_{mon}}$
$P4^{\phi}$							$Y^{P4}_{B_{la}}$						$-Y^{P4}_{B_{la}}$	$k^{P4} f_l \frac{c_{la} f_{B^{\phi}_{la}}}{K^{P4}_s + c_{la}}$
$P4^{\eta}$								$Y^{P4}_{B_{la}}$					$-Y^{P4}_{B_{la}}$	$k^{P4} f_l \frac{c_{la} f_{B^{\eta}_{la}}}{K^{P4}_s + c_{la}}$
$P4^{\delta}$									$Y^{P4}_{B_{la}}$				$-Y^{P4}_{B_{la}}$	$k^{P4} f_l \frac{c_{la} f_{B^{\delta}_{la}}}{K^{P4}_s + c_{la}}$
$P5$											$Y^{P5}_{B^{\phi}_{H_2a}}$		$-Y^{P5}_{B^{\phi}_{H_2a}}$	$k^{P5} f_l \frac{c_{H_2} f_{B^{\phi}_{H_2a}}}{K^{P5}_s + c_{H_2}}$
$P6$												$Y^{P6}_{B^{\phi}_{H_2m}}$	$-Y^{P6}_{B^{\phi}_{H_2m}}$	$k^{P6} f_l \frac{c_{H_2} f_{B^{\phi}_{H_2m}}}{K^{P6}_s + c_{H_2}} I_{pH}$
$P7$	$-Y^{P7}_{m}$												Y^{P7}_{m}	$k^{P7} R(c_{H_2S}, K^{P7}, \kappa^{P7}) 0.05 f_m$
$P8_{B^{\phi}_{mon}}$					-1								1	$k^{P8,\phi} R(c_{O_2}, K^{P8,\phi}, \kappa^{P8,\phi}) f_{B^{\phi}_{mon}}$
$P8_{B^{\eta}_{mon}}$						-1							1	$k^{P8,\eta} R(c_{O_2}, K^{P8,\eta}, \kappa^{P8,\eta}) f_{B^{\eta}_{mon}}$
$P8_{B^{\phi}_{la}}$							-1						1	$k^{P8,\phi} R(c_{O_2}, K^{P8,\phi}, \kappa^{P8,\phi}) f_{B^{\phi}_{la}}$
$P8_{B^{\eta}_{la}}$								-1					1	$k^{P8,\eta} R(c_{O_2}, K^{P8,\eta}, \kappa^{P8,\eta}) f_{B^{\eta}_{la}}$
$P8_{B^{\phi}_{H_2a}}$											-1		1	$k^{P8,\phi} R(c_{O_2}, K^{P8,\phi}, \kappa^{P8,\phi}) f_{B^{\phi}_{H_2a}}$
$P8_{B^{\phi}_{H_2m}}$												-1	1	$k^{P8,\phi} R(c_{O_2}, K^{P8,\phi}, \kappa^{P8,\phi}) f_{B^{\phi}_{H_2m}}$
$P9_{B^{\phi}_{mon}}$					-1								1	$k^{P9} R(c_{AMPs}, K^{P9}, \kappa^{P9}) f_{B^{\phi}_{mon}}$
$P9_{B^{\eta}_{mon}}$						-1							1	$k^{P9} R(c_{AMPs}, K^{P9}, \kappa^{P9}) f_{B^{\eta}_{mon}}$
$P9_{B^{\phi}_{la}}$							-1						1	$k^{P9} R(c_{AMPs}, K^{P9}, \kappa^{P9}) f_{B^{\phi}_{la}}$
$P9_{B^{\eta}_{la}}$								-1					1	$k^{P9} R(c_{AMPs}, K^{P9}, \kappa^{P9}) f_{B^{\eta}_{la}}$
$P9_{B^{\delta}_{la}}$									-1				1	$k^{P9} R(c_{AMPs}, K^{P9}, \kappa^{P9}) f_{B^{\delta}_{la}}$
$P9_{B^{\delta}_{H_2s}}$										-1			1	$k^{P9} R(c_{AMPs}, K^{P9}, \kappa^{P9}) f_{B^{\delta}_{H_2s}}$
$P9_{B^{\phi}_{H_2a}}$											-1		1	$k^{P9} R(c_{AMPs}, K^{P9}, \kappa^{P9}) f_{B^{\phi}_{H_2a}}$
$P9_{B^{\phi}_{H_2m}}$												-1	1	$k^{P9} R(c_{AMPs}, K^{P9}, \kappa^{P9}) f_{B^{\phi}_{H_2m}}$
$P10_{B^{\phi}_{mon}}$					-1								1	$k^{P10} f_{B^{\phi}_{mon}}$
$P10_{B^{\eta}_{mon}}$						-1							1	$k^{P10} f_{B^{\eta}_{mon}}$
$P10_{B^{\phi}_{la}}$							-1						1	$k^{P10} f_{B^{\phi}_{la}}$
$P10_{B^{\eta}_{la}}$								-1					1	$k^{P10} f_{B^{\eta}_{la}}$
$P10_{B^{\delta}_{la}}$									-1				1	$k^{P10} f_{B^{\delta}_{la}}$
$P10_{B^{\delta}_{H_2s}}$										-1			1	$k^{P10} f_{B^{\delta}_{H_2s}}$
$P10_{B^{\phi}_{H_2a}}$											-1		1	$k^{P10} f_{B^{\phi}_{H_2a}}$
$P10_{B^{\phi}_{H_2m}}$												-1	1	$k^{P10} f_{B^{\phi}_{H_2m}}$

Table B.4: Peterson matrix $(P_c)^t$ and kinetic rate vector K_c.

Process	mon	la	ac	pro	but	$AMPs$	H_2S	CH_4	CO_2	H_2	O_2	Kinetic K_c
$P1_m^{\phi}$	Y_{mon}^{P1}											$k^{P1}\frac{0.05\times f_m f_{B_{mon}^{\eta}}}{K_f^{P1} f_{B_{mon}^{\eta}}+0.05\times f_m} K_f^{P1}$
$P1_m^{\eta}$	Y_{mon}^{P1}											$k^{P1}\frac{0.05\times f_m f_{B_{mon}^{\eta}}}{K_f^{P1} f_{B_{mon}^{\eta}}+0.05\times f_m} K_f^{P1}$
$P1_{pol}^{\phi}$	Y_{mon}^{P1}											$k^{P1}\frac{0.05\times f_m f_{B_{mon}^{\phi}}}{K_f^{P1} f_{B_{mon}^{\phi}}+0.05\times f_m} K_f^{P1}$
$P1_{pol}^{\eta}$	Y_{mon}^{P1}											$k^{P1}\frac{0.05\times f_m f_{B_{mon}^{\eta}}}{K_f^{P1} f_{B_{mon}^{\eta}}+0.05\times f_m} K_f^{P1}$
$P2_m$							$Y_{H_2S}^{P2_m}$		$Y_{CO_2}^{P2}$	$Y_{H_2}^{P2}$	$Y_{O_2}^{P2}$	$k^{P2} f_l \frac{0.05\times f_m f_{B_{H_{2s}}^{\delta}}}{K_f^{P2} f_{B_{H_{2s}}^{\delta}}+0.05\times f_m}$
$P2_{prot}$							$Y_{H_2S}^{P2_{prot}}$		$Y_{CO_2}^{P2}$	$Y_{H_2}^{P2}$	$Y_{O_2}^{P2}$	$k^{P2} f_l \frac{f_{prot} f_{B_{H_{2s}}^{\delta}}}{K_f^{P2} f_{B_{H_{2s}}^{\delta}}+f_{prot}}$
$P3^{\phi}$	-1	Y_{la}^{P3}	Y_{ac}^{P3}	Y_{pro}^{P3}	Y_{but}^{P3}				$Y_{CO_2}^{P3}$	$Y_{H_2}^{P3}$		$k^{P3} f_l \frac{c_{mon} f_{B_{mon}^{\phi}}}{K_s^{P3}+c_{mon}}$
$P3^{\eta}$	-1	Y_{la}^{P3}	Y_{ac}^{P3}	Y_{pro}^{P3}	Y_{but}^{P3}				$Y_{CO_2}^{P3}$	$Y_{H_2}^{P3}$		$k^{P3} f_l \frac{c_{mon} f_{B_{mon}^{\eta}}}{K_s^{P3}+c_{mon}}$
$P4^{\phi}$		-1	Y_{ac}^{P4}	Y_{pro}^{P4}	Y_{but}^{P4}				$Y_{CO_2}^{P4}$	$Y_{H_2}^{P4}$		$k^{P4} f_l \frac{c_{la} f_{B_{la}^{\phi}}}{K_s^{P4}+c_{la}}$
$P4^{\eta}$		-1	Y_{ac}^{P4}	Y_{pro}^{P4}	Y_{but}^{P4}				$Y_{CO_2}^{P4}$	$Y_{H_2}^{P4}$		$k^{P4} f_l \frac{c_{la} f_{B_{la}^{\eta}}}{K_s^{P4}+c_{la}}$
$P4^{\delta}$		-1	Y_{ac}^{P4}	Y_{pro}^{P4}	-				$Y_{CO_2}^{P4}$	$Y_{H_2}^{P4}$	$Y_{O_2}^{P4}$	$k^{P4} f_l \frac{c_{la} f_{B_{la}^{\delta}}}{K_s^{P4}+c_{la}}$
$P5$			Y_{ac}^{P5}						$Y_{CO_2}^{P5}$	-1		$k^{P5} f_l \frac{c_{H_2} f_{B_{H_{2a}}^{\phi}}}{K_s^{P5}+c_{H_2}}$
$P6$								$Y_{CH_4}^{P6}$	$Y_{CO_2}^{P6}$	-1		$k^{P6} f_l \frac{c_{H_2} f_{B_{H_{2m}}^{\phi}}}{K_s^{P6}+c_{H_2}} I_{pH}$
$P11_{H_2S}$							-1					$k^{P11}(c_{H_2S} - K_{H_2S}^{P11} RT[H_2S_g]_{\infty})$
$P11_{CH_4}$								-1				$k^{P11}(c_{CH_4} - K_{CH_4}^{P11} RT[CH_{4,g}]_{\infty})$
$P11_{CO_2}$									-1			$k^{P11}(c_{CO_2} - K_{CO_2}^{P11} RT[CO_{2,g}]_{\infty})$
$P11_{H_2}$										-1		$k^{P11}(c_{H_2} - K_{H_2}^{P11} RT[H_{2,g}]_{\infty})$

Appendix B.3. Crypt geometry

From [40] we recall the curvature effect $\varphi(z)$ function :

$$\varphi(z) = \begin{cases} \frac{\frac{\tilde{f}(z)}{r_0} - \frac{\tilde{f}(0)}{r_0}}{1 - \frac{\tilde{f}(0)}{r_0}} & \text{si } z \leq r_0 - \epsilon, \\ 1 & \text{si } r_0 - \epsilon < z < Z_{max} - r_0 + \epsilon, \\ \frac{\frac{\tilde{f}(Z_{max})}{r_0} - \frac{\tilde{f}(z)}{r_0}}{\frac{\tilde{f}(Z_{max})}{r_0} - 1} & \text{si } Z_{max} - r_0 + \epsilon \leq z, \end{cases} \tag{B.3}$$

with $\tilde{f}(z)$ the function used to model crypt geometry as a truncated-tube, with a radius given by :

$$\tilde{f}(z) = \begin{cases} r_0\sqrt{\frac{z+\epsilon}{r_0}\left(2-\frac{z+\epsilon}{r_0}\right)} & \text{is } z \leq r_0 - \epsilon, \\ r_0 & \text{if } r_0 - \epsilon < z < Z_{max} - r_0 + \epsilon, \\ r_0\left(2 - \sqrt{\frac{Z_{max}-z+\epsilon}{r_0}\left(2-\frac{Z_{max}-z+\epsilon}{r_0}\right)}\right) & \text{if } Z_{max} - r_0 + \epsilon \leq z. \end{cases} \tag{B.4}$$

Appendix B.4. Cell fate events and their regulations

Complete formulation of Q_k present in Eq. 16, based on the regulatory pathways illustrated in Table 2 and using the $R(.)$ activation function Eq. 8.

For stem cells :

$$\begin{aligned} Q_{div,sc}(\ell, z, \rho(z), \tilde{c}_{but}(z), f_B) =& \mathbb{1}_{\{\ell=sc\}}(1 - R(z, K_{div,sc}[z], \kappa_{div,sc}[z])) \\ & \times (1 - R(D\rho(z,t), K_{div,sc}[dens], \kappa_{div,sc}[dens]) \\ & \times (1 - R(\tilde{c}_{but}(z), K_{div,sc}[but], \kappa_{div,sc}[but])) \\ & \times (R(f_B, K_{div,sc}[PRRs], \kappa_{div,sc}[PRRs])). \\ Q_{sc,pc}(\ell, z) =& \mathbb{1}_{\{\ell=sc\}} R(z, K_{sc,pc}[z], \kappa_{sc,pc}[z]). \end{aligned} \tag{B.5}$$

For progenitor cells :

$$\begin{aligned} Q_{div,pc}(\ell, z, \rho(z), f_B) =& \mathbb{1}_{\{\ell=pc\}}(1 - R(z, K_{div,pc}[z], \kappa_{div,pc}[z])) \\ & \times (1 - R(D\rho(z), K_{div,pc}[dens], \kappa_{div,pc}[dens]) \\ & \times (R(f_B, K_{div,pc}[PRRs], \kappa_{div,pc}[PRRs])). \\ Q_{pc,gc}(\ell, z, \tilde{c}_{but}(z)) =& \mathbb{1}_{\{\ell=pc\}} R(z, K_{pc,gc}[z], \kappa_{pc,gc}[z]) \\ & \times R(\tilde{c}_{but}(z), K_{pc,gc}[but], \kappa_{pc,gc}[but]). \\ Q_{pc,ent}(\ell, z, \tilde{c}_{but}(z)) =& \mathbb{1}_{\{\ell=pc\}} R(z, K_{pc,ent}[z], \kappa_{pc,ent}[z]) \\ & \times R(\tilde{c}_{but}(z), K_{pc,ent}[but], \kappa_{pc,ent}[but]). \end{aligned} \tag{B.6}$$

For goblet cells and enterocytes :

$$\begin{aligned} Q_{ex,gc}(\ell, z, \rho(z)) =& \mathbb{1}_{\{\ell=gc\}} R(z, K_{ex,gc}[z], \kappa_{ex,gc}[z])) \\ & \times R(D\rho(z), K_{ex,gc}[dens], \kappa_{ex,gc}[dens]). \\ Q_{ex,ent}(\ell, z, \rho(z)) =& \mathbb{1}_{\{\ell=ent\}} R(z, K_{ex,ent}[z], \kappa_{ex,ent}[z])) \\ & \times R(D\rho(z), K_{ex,ent}[dens], \kappa_{ex,ent}[dens]). \end{aligned} \tag{B.7}$$

Appendix B.5. DCS cells density shape

Following [40], DCS cells density is given by :

$$\rho_{dcs}(z) = \frac{N_{dcs}}{\int_0^{Z_{max}} \bar{\rho}_{dcs}(z)dz} \bar{\rho}_{dcs}(z) \tag{B.8}$$

Where $\bar{\rho}_{dcs}(z)$ is a piecewise-linear approximation of a step-function governed by four shape parameters: $d > 0$, $u < 0$, z_d, and z_u :

$$\bar{\rho}_{dcs}(z) = \begin{cases} d(z - z_d) + 1 & \text{if } z_d - \frac{1}{d} < z < z_d, \\ 1 & \text{if } z_d \leq z \leq z_u, \\ 1 + u(z - z_u) & \text{if } z_u < z < z_u - \frac{1}{u}, \\ 0 & \text{otherwise.} \end{cases}$$

Appendix C. Model parameters

Table C.5: Colon model parameters

Parameter	Value	Unit	Description	Refs
		Maximum specific reaction rates		
k^{P1}	50	h^{-1}	Max. specific reaction rate for P1	[21]
k^{P2_m}	2.92	h^{-1}	Max. specific reaction rate for $P2_m$	-
$k^{P2_{prot}}$	3.75	h^{-1}	Max. specific reaction rate for $P2_{prot}$	-
k^{P3}	0.33	h^{-1}	Max. specific reaction rate for P3	[21]
k^{P4}	4.33	h^{-1}	Max. specific reaction rate for P4	[21]
k^{P5}	4.53	h^{-1}	Max. specific reaction rate for P5	[21]
k^{P6}	0.94	h^{-1}	Max. specific reaction rate for P6	[21]
k^{P7}	1×10^{-4}	h^{-1}	Max. specific reaction rate for P7	-
$k^{P8,\phi}$	0.02	h^{-1}	Max. specific reaction rate for P8	-
$k^{P8,\eta}$	0.04	h^{-1}	Max. specific reaction rate for P8	-

Table C.5 – Continued

Parameter	Value	Unit	Description	Refs
k^{P9}	0.02	h^{-1}	Max. specific reaction rate for P9	-
k^{P10}	4×10^{-4}	h^{-1}	Max. specific reaction rate for P10	[21]
k^{P11}	8.33	h^{-1}	Max. specific reaction rate for P11	[21]
		Half saturation constant		
K_f^{P1}	29 /113	[-]	Comtois law	[21]
K_f^{P2}	50/113	[-]	Comtois law	-
K_s^{P3}	2×10^{-6}	$mol.cm^{-3}$	Monod law	[21]
K_s^{P4}	6.626×10^{-6}	$mol.cm^{-3}$	Monod law	[21]
K_s^{P5}	1.7×10^{-6}	$mol.cm^{-3}$	Monod law	[21]
K_s^{P6}	1.563×10^{-6}	$mol.cm^{-3}$	Monod law	[21]
		Toxicity parameters		
K^{P7}	0.7×10^{-6}	$mol.cm^{-3}$	activ. parameter for P7	-
κ^{P7}	0.6×10^{-6}	$mol.cm^{-3}$	activ. parameter for P7	-
$K^{P8,\phi}$	3.5	$[a.u]$	activ. parameter for P8	-
$\kappa^{P8,\phi}$	0.5	$[a.u]$	activ. parameter for P8	-
$K^{P8,\eta}$	4	$[a.u]$	activ. parameter for P8	-
$\kappa^{P8,\eta}$	1	$[a.u]$	activ. parameter for P8	-
K^{P9}	4×10^{-8}	$mol.cm^{-3}$	activ. parameter for P9	-
κ^{P9}	2.5×10^{-8}	$mol.cm^{-3}$	activ. parameter for P9	-
		pH influence		
I_{pH}^{trans}	8.496×10^{-2}	[-]	pH influence for P6	[20]
		Focus on process 11		
$K_{H_2S}^{P11}$	7.29×10^{-4}	$mol.bar^{-1}$	Henry's law coef.	-
$K_{CH_4}^{P11}$	0.0011	$mol.bar^{-1}$	Henry's law coef.	[21]
$K_{CO_2}^{P11}$	0.0255	$mol.bar^{-1}$	Henry's law coef.	[21]
$K_{H_2}^{P11}$	7.29×10^{-4}	$mol.bar^{-1}$	Henry's law coef.	[21]
R	0.08314	$bar.mol^{-1}.K^{-1}$	Ideal gaz constant	[21]
T	310.15	K	Gas absolute temperature	[21]

Table C.5 – Continued

Parameter	Value	Unit	Description	Refs
$[H_2S_g]_\infty$	3.6505×10^{-7}	$mol.cm^{-3}$	Gaseous CH_4 steady state level	-
$[CH_{4,g}]_\infty$	1.9106×10^{-10}	$mol.cm^{-3}$	Gaseous CH_4 steady state level	[21]
$[CO_{2,g}]_\infty$	1.19×10^{-5}	$mol.cm^{-3}$	Gaseous CO_2 steady state level	[21]
$[H_{2,g}]_\infty$	3.6505×10^{-7}	$mol.cm^{-3}$	Gaseous H_2 steady state level	[21]
		Process P1		
Y_m^{P1}	8.850×10^{-3}	[-]	Yield of m in process 1	[21]
Y_{pol}^{P1}	8.850×10^{-3}	[-]	Yield of pol in process 1	[21]
Y_{mon}^{P1}	4.425×10^{-5}	$mol.cm^{-3}$	Production yield of mon in process 1	[21]
		Process P2		
Y_m^{P2}	8.850×10^{-3}	[-]	Yield of m in process 2	-
Y_{prot}^{P2}	8.850×10^{-3}	[-]	Yield of $prot$ in process 2	-
$Y_{B_{H_2s}^\delta}^{P2_m}$	0.001	$mol.cm^{-3}$	Production yield of $B_{H_2S}^\delta$ in process 2 specific to mucoproteins	-
$Y_{B_{H_2s}^\delta}^{P2_{prot}}$	0.01	$mol.cm^{-3}$	Production yield of $B_{H_2S}^\delta$ in process 2 specific to proteins	-
$Y_{H_2S}^{P2_m}$	7.08×10^{-5}	$mol.cm^{-3}$	Production yield of H_2S in process 2 specific to mucoproteins	-
$Y_{H_2S}^{P2_{prot}}$	1.33×10^{-3}	$mol.cm^{-3}$	Production yield of H_2S in process 2 specific to proteins	-
$Y_{H_2}^{P2}$	-2.83×10^{-4}	$mol.cm^{-3}$	yield of H_2 in process 2	-
$Y_{O_2}^{P2}$	-200	$[a.u]$	Yield of O_2 in process 2	-
$Y_{CO_2}^{P2}$	-7.08×10^{-5}	$mol.cm^{-3}$	Yield of CO_2 in process 2	-
		Process P3		
Y_{mon}^{P3}	8.850×10^{-3}	$mol.cm^{-3}$	Degradation yield of mon in process 3	[21]

Table C.5 – Continued

Parameter	Value	Unit	Description	Refs
$Y_{B_{mon}}^{P3}$	0.120	[-]	Biomass yield factor for B_{mon}	[21]
Y_{la}^{P3}	4.416×10^{-3}	$mol.cm^{-3}$	Production yield of la in process 3	[21]
Y_{ac}^{P3}	5.18×10^{-3}	$mol.cm^{-3}$	Production yield of ac in process 3	[21]
Y_{pro}^{P3}	2.124×10^{-3}	$mol.cm^{-3}$	Production yield of pro in process 3	[21]
Y_{but}^{P3}	2.389×10^{-3}	$mol.cm^{-3}$	Production yield of but in process 3	[21]
$Y_{CO_2}^{P3}$	9.735×10^{-3}	$mol.cm^{-3}$	Production yield of CO_2 in process 3	[21]
$Y_{H_2}^{P3}$	1.274×10^{-2}	$mol.cm^{-3}$	Production yield of H_2 in process 3	[21]
		Process P4		
Y_{la}^{P4}	8.850×10^{-3}	$mol.cm^{-3}$	Degradation yield of la in process 4	[21]
$Y_{B_{la}}^{P4}$	0.120	[-]	Biomass yield factor for B_{la}	[21]
Y_{ac}^{P4}	1.177×10^{-3}	$mol.cm^{-3}$	Production yield of ac in process 4	[21]
Y_{pro}^{P4}	2.363×10^{-3}	$mol.cm^{-3}$	Production yield of pro in process 4	[21]
Y_{but}^{P4}	1.770×10^{-3}	$mol.cm^{-3}$	Production yield of but in process 4	[21]
$Y_{CO_2}^{P4}$	4.717×10^{-3}	$mol.cm^{-3}$	Production yield of CO_2 in process 4	[21]
$Y_{H_2}^{P4}$	3.540×10^{-2}	$mol.cm^{-3}$	Production yield of H_2 in process 4	[21]
$Y_{O_2}^{P4}$	-300	$[a.u]$	Production yield of but in process 4	[21]
		Process P5		
$Y_{H_2}^{P5}$	8.850×10^{-3}	$mol.cm^{-3}$	Degradation yield of H_2 in process 5	[21]
$Y_{B_{H_2a}^{\phi}}^{P5}$	0.043	[-]	Biomass yield factor for $B_{H_2a}^{\phi}$	[21]

Table C.5 – Continued

Parameter	Value	Unit	Description	Refs
Y_{ac}^{P5}	2.21×10^{-3}	$mol.cm^{-3}$	Production yield of ac in process 5	[32]
$Y_{CO_2}^{P5}$	-4.424×10^{-3}	$mol.cm^{-3}$	Yield of CO_2 in process 5	[21]
		Process P6		
$Y_{H_2}^{P6}$	8.850×10^{-3}	$mol.cm^{-3}$	Degradation yield of H_2 in process 6	[21]
$Y_{B_{H_2m}^{\phi}}^{P6}$	0.062	[-]	Biomass yield factor for $B_{H_2m}^{\phi}$	[21]
$Y_{CH_4}^{P6}$	8.407×10^{-4}	$mol.cm^{-3}$	Production yield of CH_4 in process 6	[21]
$Y_{CO_2}^{P6}$	-3.982×10^{-3}	$mol.cm^{-3}$	Yield of CO_2 in process 6	[21]
Y_{m}^{P7}	8.850×10^{-3}	[–]	Yield of m in process 7	[21]
		Colon geometry		
L	1	cm	Section length	-
R	2.5	cm	Colon radius	[20]
e_m	0.0830	cm	Mucus thickness	[21]
e_m^O	$= 3/4e_m$	cm	Inner mucus thickness	-
e_m^I	$= 1/4e_m$	cm	Inner mucus thickness	-
Γ^{in}	18.35	cm^2	Input surface of the lumen	-
Γ^{out}	$= \Gamma^{in}$	cm^2	Output surface of the lumen (L)	-
Γ^L	15.19	cm^2	Interface between L and Outer mucus (O)	-
Γ^O	15.58	cm^2	Interface between O and Inner mucus (I)	-
Γ^I	15.71	cm^2	Interface between Is and epithelium	-
V^L	18.35	cm^3	L volume	-
V^O	0.96	cm^3	O volume	-
V^I	0.32	cm^3	I volume	-
		Colon flows		
v_{mon}	0.396	$cm.h^{-1}$	Monosaccharides diffusion rate	-
v_{CH_4}	0.333	$cm.h^{-1}$	CH_4 diffusion rate	-

Table C.5 – Continued

Parameter	Value	Unit	Description	Refs
v_{CO_2}	$= q_{CH_4}$	$cm.h^{-1}$	CO_2 diffusion rate	-
v_{H_2}	$= q_{CH_4}$	$cm.h^{-1}$	H_2 diffusion rate	-
$v_{la}^{L,O}$	1.044×10^{-6}	$cm.h^{-1}.cell^{-1}$	Lactate absorption rate trough Γ^L	-
$v_{ac}^{L,O}$	4.178×10^{-6}	$cm.h^{-1}.cell^{-1}$	Acetate absorp. rate trough Γ^L	-
$v_{pro}^{L,O}$	4.178×10^{-6}	$cm.h^{-1}.cell^{-1}$	Propionate absorp. rate trough Γ^L	-
$v_{but}^{L,O}$	3.133×10^{-6}	$cm.h^{-1}.cell^{-1}$	Butyrate absorp. rate trough Γ^L	-
$v_{H_2S}^{L,O}$	1.566×10^{-5}	$cm.h^{-1}.cell^{-1}$	H_2S absorp. rate trough Γ^L	-
$v_{la}^{O,I}$	3.133×10^{-6}	$cm.h^{-1}.cell^{-1}$	Lactate absorption rate trough Γ^O and Γ^I	-
$v_{ac}^{O,I}$	6.266×10^{-6}	$cm.h^{-1}.cell^{-1}$	Acetate absorp. rate trough $\Gamma^L$and Γ^I	-
$v_{pro}^{O,I}$	6.266×10^{-6}	$cm.h^{-1}.cell^{-1}$	Propionate absorp. rate trough $\Gamma^L$and Γ^I	-
$v_{but}^{O,I}$	5.222×10^{-6}	$cm.h^{-1}.cell^{-1}$	Butyrate absorp. rate trough $\Gamma^L$and Γ^I	-
$v_{H_2S}^{O,I}$	1.566×10^{-5}	$cm.h^{-1}.cell^{-1}$	H_2S absorp. rate trough $\Gamma^L$and Γ^I	-
$v_l^{I,E}$	6.621×10^{-6}	$cm.h^{-1}.cell^{-1}$	Liquid absorp. rate between I and epithelium	-
$v_l^{O,I}$	$= q_l^I/10$	$cm.h^{-1}.cell^{-1}$	Liquid absorp. rate between O and I	-
$v_l^{L,O}$	$= q_l^{O,I}$	$cm.h^{-1}.cell^{-1}$	Liquid absorp. rate between L and O	-
v_{O_2}	0.036	$cm.h^{-1}$	O_2 diffusion rate between L and O	[40]
$v_{O_2}^{O,L}$	$= q_{O_2}$	$cm.h^{-1}$	O_2 diffusion rate between O and L	-
$v_{O_2}^{I,O}$	$= q_{O_2}$	$cm.h^{-1}$	O_2 diffusion rate between I and O	-
v_{AMPs}	7.519×10^{-15}	$cm.h^{-1}.cell^{-1}$	Basal AMPs production rate	-

Table C.5 – Continued

Parameter	Value	Unit	Description	Refs
$v_{AMPs}^{I,O}$	5×10^{-4}	$cm.h^{-1}$	AMPs diffusion rate between I and O	-
$v_{AMPs}^{O,L}$	5×10^{-3}	$cm.h^{-1}$	AMPs diffusion rate between O and L	-
v_m	1.579×10^{-6}	$cm.h^{-1}.cell^{-1}$	Mucus production rate	-
θ	0.3	[–]	Proportion of basal mucus and AMPs production	–
a	0.00042	$cm.h^{-1}$	Microbial adherence rate	-
b	0.0033	[–]	Microbial shear coefficient	Adapted [21]
τ	0.0416	$cm.h^{-1}$	Microbial residence coefficient	Adapted [21]
		Input on Γ^{in}		
f_m^{in}	0	[-]	Mucus density input	
f_{pol}^{in}	0.05	[-]	Polysaccharide density input	[21]
f_{prot}^{in}	0.0135	[-]	Protein density input	-
$f_{B_{mon}^{\phi}}^{in}$	$1.68 \times 10^{-3} \times 3/4$	[-]	B_{mon}^{ϕ} density input	graph. read. [20]
$f_{B_{mon}^{\eta}}^{in}$	$1.68 \times 10^{-3} \times 1/4$	[-]	B_{mon}^{η} density input	graph. read. [20]
$f_{B_{la}^{\phi}}^{in}$	$7.8 \times 10^{-4} \times 4/7$	[-]	B_{la}^{ϕ} density input	graph. read. [20]
$f_{B_{la}^{\eta}}^{in}$	$7.8 \times 10^{-4} \times 2/7$	[-]	B_{la}^{η} density input	graph. read. [20]
$f_{B_{la}^{\delta}}^{in}$	$7.8 \times 10^{-4} \times 1/7$	[-]	B_{la}^{δ} density input	graph. read. [20]
$f_{B_{H_2s}^{\delta}}^{in}$	2×10^{-4}	[-]	$B_{H_2s}^{\delta}$ density input	-
$f_{B_{H_2a}^{\phi}}^{in}$	4.5×10^{-4}	[-]	$B_{H_2a}^{\phi}$ density input	graph. read. [20]
$f_{B_{H_2m}^{\phi}}^{in}$	8.9×10^{-5}	[-]	$B_{H_2m}^{\phi}$ density input	graph. read. [20]
f_r^{in}	0.05	[-]	Digestible residuals density input	[20]
c_{mon}^{in}	3.33×10^{-5}	$mol.cm^{-3}$	Monosaccharide density input	[20]

Table C.5 – Continued

Parameter	Value	Unit	Description	Refs
c_{la}^{in}	3×10^{-6}	$mol.cm^{-3}$	Lactate density input	graph. read.[20]
c_{ac}^{in}	6×10^{-5}	$mol.cm^{-3}$	Acetate density input	graph. read. [20]
c_{pro}^{in}	2×10^{-5}	$mol.cm^{-3}$	Propionate density input	graph. read.[20]
c_{but}^{in}	2×10^{-5}	$mol.cm^{-3}$	Butyrate density input	graph. read.[20]
$c_{CH_4}^{in}$	1×10^{-7}	$mol.cm^{-3}$	Methane density input	-
$c_{CO_2}^{in}$	1×10^{-7}	$mol.cm^{-3}$	Carbon dioxide density input	-
$c_{H_2}^{in}$	1×10^{-7}	$mol.cm^{-3}$	Hydrogen density input	-
$c_{H_2s}^{in}$	1×10^{-6}	$mol.cm^{-3}$	Hydrogen sulfur density input	-
$c_{O_2}^{in}$	1	[a.u]	Oxygen density input	-
c_{AMPs}^{in}	1×10^{-8}	$mol.cm^{-3}$	AMPs density input	-

Table C.6: Crypt model parameters

Parameter	Value	Unit	Description	Refs
		Crypt geometry		
Z_{max}	400	μm	Height	[49]
r_0	37	μm	Radius	[49]
ϵ	4	μm	Shape parameter	-
		Metabolites $\beta-$oxidation parameters		
$s_{o,la}$	3	-	O_2 stoichiometric coefficient during lactate consumption	-
$s_{o,ac}$	7/2	-	O_2 stoic. coef. during acetate consumption	-
$s_{o,pro}$	7/2	-	O_2 stoic. coef. during propionate consumption	-
$s_{o,but}$	7/2	-	O_2 stoic. coef. during butyrate consumption	-
s_{la}	1	-	Lactate stoic. coef.	-

Table C.6 – Continued

Parameter	Value	Unit	Description	Refs
s_{ac}	1	-	Acetate stoic. coef.	-
s_{pro}	1	-	Propionate stoic. coef.	-
s_{but}	1	-	Butyrate stoic. coef.	-
γ_{la}^{β}	0	$10^{-15} \times \frac{mmol}{h \times \mu m^2}$	Max. reaction speed	-
γ_{ac}^{β}	$= \gamma_{la}^{\beta}$	$10^{-15} \times \frac{mmol}{h \times \mu m^2}$	Max. reaction speed	-
γ_{pro}^{β}	$= \gamma_{la}^{\beta}$	$10^{-15} \times \frac{mmol}{h \times \mu m^2}$	Max. reaction speed	-
γ_{but}^{β}	2.2×10^2	$10^{-15} \times \frac{mmol}{h \times \mu m^2}$	Max. reaction speed	-
K_{la}	$(2e^3)^{2/7}$	mM	Affinity of β-oxydation	-
K_{ac}	$(2e^3)^{2/7}$	mM	Affinity of β-oxydation	-
K_{pro}	$(2e^3)^{2/7}$	mM	Affinity of β-oxydation	-
K_{but}	$(9e^3)^{2/7}$	mM	Affinity of β-oxydation	-
K_{HIF}	1.5	mM	Butyrate activation of β-oxyd.	-
l_{HIF}	0.5	mM	Butyrate activation of β-oxyd.	-
K_{H_2S}	0.05	mM	H_2S inhibition of β-oxyd.	-
l_{H_2S}	0.001	mM	H_2S inhibition of β-oxyd.	-
Metabolites absorption parameters				
γ_{la}^{α}	70	h^{-1}	Lactate absorption rate	-
γ_{ac}^{α}	78	h^{-1}	Acetate absorption rate	-
γ_{pro}^{α}	95	h^{-1}	Propionate absorption rate	-
γ_{but}^{α}	70	h^{-1}	Butyrate absorption rate	-
Concentration diffusion coefficients and boundary condition				
σ_o	$3.6e^6$	$\mu m^2/h$	O_2 diffusion coef.	[40]
σ_{la}	$= \sigma_o$	$\mu m^2/h$	Lactate diffusion coef.	-
σ_{ac}	$= \sigma_o$	$\mu m^2/h$	Acetate diffusion coef.	-
σ_{pro}	$= \sigma_o$	$\mu m^2/h$	Propionate diffusion coef.	-
σ_{but}	$= \sigma_o$	$\mu m^2/h$	Butyrate diffusion coef.	[40]
Cell interaction parameters				
W	6.01/8	-	Interaction force	[40]
D	8	-	Local density effect on cells	-
DCS cell density shape				
N_{dcs}	36	-	Number of DCS cells	-

Table C.6 – Continued

Parameter	Value	Unit	Description	Refs
z_d	6	μm	Shape parameter	-
d	20	μm	Shape parameter	-
z_u	3	μm	Shape parameter	-
u	1/15	μm	Shape parameter	-
Boundary conditions at the bottom of the crypt for densities				
ρ_{sc}^{bot}	0.6		Stem cell dentity	-
ρ_{pc}^{bot}	0		Progenitor cell dentity	-
ρ_{gc}^{bot}	0		Goblet cell dentity	-
ρ_{ent}^{bot}	0		Enterocyte cell dentity	-
Boundary conditions at the bottom of the crypt for densities				
$\tilde{c_o}^{bot}$	48.8	[a.u]	Oxygen concentration	-
Cell fate event regulation for stem cells (sc)				
$q_{div,sc}$	0.15	h^{-1}	Max. division rate of sc	[40]
$K_{div,sc}[z]$	24	μm	Space-reg. for sc div.	-
$\kappa_{div,sc}[z]$	5	μm	Space-related reg. for sc div.	-
$K_{div,sc}[dens]$	53	$cell$	Density-reg. for sc div.	[40]
$\kappa_{div,sc}[dens]$	6	$cell$	Density-related reg. for sc div.	[40]
$K_{div,sc}[but]$	1	-	Butyrate-related reg. for sc div.	-
$\kappa_{div,sc}[but]$	5	-	Butyrate-related reg. for sc div.	-
$K_{div,sc}[PRRs]$	0.003	-	PRRs-related reg. for sc div.	-
$\kappa_{div,sc}[PRRs]$	0.003	-	PRRs-related reg. for sc div.	-
$q_{sc,pc}$	0.2	h^{-1}	Mac. differentiation rate of sc	[40]
$K_{sc,pc}[z]$	$= K_{div,sc}[z]$	μm	Space-reg. for sc diff.	-
$\kappa_{sc,pc}[z]$	$= \kappa_{div,sc}[z]$	μm	Space-related reg. for sc diff.	-
Cell fate event regulation for progenitor cells (pc)				
$q_{div,pc}$	0.22	h^{-1}	Max division rate of pc cells	-
$K_{div,pc}[z]$	110	μm	Space-reg. for pc div.	-
$\kappa_{div,pc}[z]$	40	μm	Space-related reg. for pc div.	-
$K_{div,pc}[dens]$	41	$cell$	Density-reg. for pc div.	[40]
$\kappa_{div,pc}[dens]$	$= \kappa_{div,sc}[dens]$	$cell$	Density-related reg. for pc div.	[40]
$K_{div,pc}[PRRs]$	$= K_{div,sc}[PRRs]$	-	PRRs-related reg. for pc div.	-

Table C.6 – Continued

Parameter	Value	Unit	Description	Refs
$\kappa_{div,pc}[PRRs]$	$= \kappa_{div,sc}[PRRs]$	-	PRRs-related reg. for *pc* div.	-
$q_{pc,gc}$	$= q_{pc,ent}/3$	h^{-1}	Max. differentiation rate of *pc* in goblet cells	[40]
$K_{pc,gc}[z]$	$= K_{div,pc}[z]$	μm	Space-reg. for *pc* diff. in *gc*	-
$\kappa_{pc,gc}[z]$	15	μm	Space-reg. for *pc* diff. in *gc*	-
$K_{pc,gc}[but]$	0.8	-	Butyrate-related reg. for *pc* diff. in *gc*	-
$\kappa_{pc,gc}[but]$	0.5	-	Butyrate-related reg. for *pc* diff. in *gc*	-
$q_{pc,ent}$	0.25	h^{-1}	Max diff. rate of *pc* in enterocyte	[40]
$K_{pc,ent}[z]$	$= K_{div,pc}[z]$	μm	Space-reg. for *pc* diff. in *ent*	-
$\kappa_{pc,ent}[z]$	$= \kappa_{pc,gc}[z]$	μm	Space-reg. for *pc* diff. in *ent*	-
$K_{pc,ent}[but]$	$K_{pc,gc}[but]$	-	Butyrate-related reg. for *pc* diff. in *ent*	-
$\kappa_{pc,ent}[but]$	$\kappa_{pc,gc}[but]$	-	Butyrate-related reg. for *pc* diff. in *ent*	-
Cell fate event regulation for goblet cells (*gc*)				
$q_{ex,gc}$	0.34	h^{-1}	Max rate of extrusion	[40]
$K_{ex,gc}[z]$	380	μm	Space-reg. for *gc* ext.	-
$\kappa_{ex,gc}[z]$	15	μm	Space-related reg. for *gc* ext.	-
$K_{ex,gc}[dens]$	20	*cell*	Density-reg. for *gc* ext.	[40]
$\kappa_{ex,gc}[dens]$	$\kappa_{div,sc}[dens]$	*cell*	Density-related reg. for *sc* div.	[40]
Cell fate event regulation for enterocyte cells (*ent*)				
$q_{ex,gc}$	$= q_{ex,gc}$	h^{-1}	Max rate of extrusion	[40]
$K_{ex,ent}[z]$	$= K_{ex,ent}[z]$	μm	Space-reg. for *gc* ext.	-
$\kappa_{ex,ent}[z]$	$\kappa_{ex,gc}[z]$	μm	Space-related reg. for *gc* ext.	-
$K_{ex,ent}[dens]$	$K_{ex,gc}[dens]$	*cell*	Density-reg. for *gc* ext.	[40]
$\kappa_{ex,ent}[dens]$	$\kappa_{div,sc}[dens]$	*cell*	Density-related reg. for *sc* div.	[40]

Funding source

Author contribution and data collection was permitted in part by funding from the European Research Council (ERC) under the European Union's Horizon 2020 research and innovation program (Grant agreement ERC-2017-AdG No. 788191 - Homo.symbiosus).

Availability of data

16S rRNA gene sequence data are available on NCBI under BioProject PRJNA986321.

References

[1] R. Sender, S. Fuchs, R. Milo, Revised Estimates for the Number of Human and Bacteria Cells in the Body, PLOS Biology 14 (8) (2016) e1002533. doi:10.1371/journal.pbio.1002533.

[2] Y. Belkaid, O. J. Harrison, Homeostatic immunity and the microbiota, Immunity 46 (4) (2017) 562–576. doi:10.1016/j.immuni.2017.04.008.

[3] F. Bäckhed, C. M. Fraser, Y. Ringel, M. E. Sanders, R. B. Sartor, P. M. Sherman, J. Versalovic, V. Young, B. B. Finlay, Defining a Healthy Human Gut Microbiome: Current Concepts, Future Directions, and Clinical Applications, Cell Host & Microbe 12 (5) (2012) 611–622. doi:10.1016/j.chom.2012.10.012.

[4] T. Liwinski, D. Zheng, E. Elinav, The microbiome and cytosolic innate immune receptors, Immunological Reviews 297 (1) (2020) 207–224. doi:10.1111/imr.12901.

[5] B. O. Schroeder, Fight them or feed them: How the intestinal mucus layer manages the gut microbiota, Gastroenterology Report 7 (1) (2019) 3–12. doi:10.1093/gastro/goy052.

[6] H. E. Jakobsson, A. M. Rodríguez-Piñeiro, A. Schütte, A. Ermund, P. Boysen, M. Bemark, F. Sommer, F. Bäckhed, G. C. Hansson, M. E. V. Johansson, The composition of the gut microbiota shapes the colon mucus barrier, EMBO reports 16 (2) (2015) 164–177. doi:10.15252/embr.201439263.

[7] C. Thaiss, N. Zmora, M. Levy, E. Elinav, The microbiome and innate immunity, Nature 535 (2016) 65–74. doi:10.1038/nature18847.

[8] D. Zheng, T. Liwinski, E. Elinav, Interaction between microbiota and immunity in health and disease, Cell Research 30 (6) (2020) 492–506. doi:10.1038/s41422-020-0332-7.

[9] W. R. Russell, S. W. Gratz, S. H. Duncan, G. Holtrop, J. Ince, L. Scobbie, G. Duncan, A. M. Johnstone, G. E. Lobley, R. J. Wallace, G. G. Duthie, H. J. Flint, High-protein, reduced-carbohydrate weight-loss diets promote metabolite profiles likely to be detrimental to colonic health, The American Journal of Clinical Nutrition 93 (5) (2011) 1062–1072. doi:10.3945/ajcn.110.002188.

[10] M. K. Zinöcker, I. A. Lindseth, The Western Diet–Microbiome-Host Interaction and Its Role in Metabolic Disease, Nutrients 10 (3) (2018) 365. doi:10.3390/nu10030365.

[11] F. Rivera-Chávez, C. A. Lopez, A. J. Bäumler, Oxygen as a driver of gut dysbiosis, Free Radical Biology and Medicine 105 (2017) 93–101. doi:10.1016/j.freeradbiomed.2016.09.022.

[12] L. P. Pral, J. L. Fachi, R. O. Corrêa, M. Colonna, M. A. R. Vinolo, Hypoxia and HIF-1 as key regulators of gut microbiota and host interactions, Trends in Immunology 42 (7) (2021) 604–621. doi:10.1016/j.it.2021.05.004.

[13] I. Garcia-Mantrana, M. Selma-Royo, C. Alcantara, M. C. Collado, Shifts on Gut Microbiota Associated to Mediterranean Diet Adherence and Specific Dietary Intakes on General Adult Population, Frontiers in Microbiology 9 (2018) 890. doi:10.3389/fmicb.2018.00890.

[14] F. De Filippis, N. Pellegrini, L. Vannini, I. B. Jeffery, A. La Storia, L. Laghi, D. I. Serrazanetti, R. Di Cagno, I. Ferrocino, C. Lazzi, S. Turroni, L. Cocolin, P. Brigidi, E. Neviani, M. Gobbetti, P. W. O'Toole, D. Ercolini, High-level adherence to a Mediterranean diet beneficially impacts the gut microbiota and associated metabolome, Gut 65 (11) (2016) 1812–1821. doi:10.1136/gutjnl-2015-309957.

[15] F. Rivera-Chávez, L. F. Zhang, F. Faber, C. A. Lopez, M. X. Byndloss, E. E. Olsan, G. Xu, E. M. Velazquez, C. B. Lebrilla, S. E. Winter, A. J. Bäumler, Depletion of Butyrate-Producing Clostridia from the Gut Microbiota Drives an Aerobic Luminal Expansion of Salmonella, Cell Host & Microbe 19 (4) (2016) 443–454. doi:10.1016/j.chom.2016.03.004.

[16] D. Parada Venegas, M. K. De la Fuente, G. Landskron, M. J. González, R. Quera, G. Dijkstra, H. J. M. Harmsen, K. N. Faber, M. A. Hermoso, Short Chain Fatty Acids (SCFAs)-Mediated Gut Epithelial and Immune Regulation and Its Relevance for Inflammatory Bowel Diseases, Frontiers in Immunology 10 (2019).

[17] R. B. Canani, M. D. Costanzo, L. Leone, M. Pedata, R. Meli, A. Calignano, Potential beneficial effects of butyrate in intestinal and extraintestinal diseases, World Journal of Gastroenterology 17 (12) (2011) 1519–1528. doi:10.3748/wjg.v17.i12.1519.

[18] C. Martin-Gallausiaux, L. Marinelli, H. M. Blottière, P. Larraufie, N. Lapaque, SCFA: Mechanisms and functional importance in the gut, Proceedings of the Nutrition Society 80 (1) (2021) 37–49. doi:10.1017/S0029665120006916.

[19] R. B. Young, V. R. Marcelino, M. Chonwerawong, E. L. Gulliver, S. C. Forster, Key Technologies for Progressing Discovery of Microbiome-Based Medicines, Frontiers in Microbiology 12 (2021).

[20] S. Labarthe, B. Polizzi, T. Phan, T. Goudon, M. Ribot, B. Laroche, A mathematical model to investigate the key drivers of the biogeography of the colon microbiota, Journal of Theoretical Biology 462 (2019) 552–581. doi:10.1016/j.jtbi.2018.12.009.

[21] R. Muñoz-Tamayo, B. Laroche, E. Walter, J. Doré, M. Leclerc, Mathematical modelling of carbohydrate degradation by human colonic microbiota, Journal of Theoretical Biology 266 (1) (2010) 189–201. doi:10.1016/j.jtbi.2010.05.040.

[22] H. Kettle, G. Holtrop, P. Louis, H. J. Flint, microPop: Modelling microbial populations and communities in R, Methods in Ecology and Evolution 9 (2) (2018) 399–409. doi:10.1111/2041-210X.12873.

[23] N. W. Smith, P. R. Shorten, E. Altermann, N. C. Roy, W. C. McNabb, Examination of hydrogen cross-feeders using a colonic microbiota model, BMC Bioinformatics 22 (1) (2021) 3. doi:10.1186/s12859-020-03923-6.

[24] J. Geng, B. Ji, G. Li, F. López-Isunza, J. Nielsen, CODY enables quantitatively spatiotemporal predictions on in vivo gut microbial variability induced by diet intervention, Proceedings of the National Academy of Sciences of the United States of America 118 (13) (2021) e2019336118. doi:10.1073/pnas.2019336118.

[25] L. Darrigade, Modélisation du dialogue hôte-microbiote au voisinage de l'épithélium de l'intestin distal, Ph.D. thesis, Université Paris-Saclay (Dec. 2020).

[26] J. Arciero, G. B. Ermentrout, R. Siggers, A. Afrazi, D. Hackam, Y. Vodovotz, J. Rubin, Modeling the interactions of bacteria and Toll-like receptor-mediated inflammation in necrotizing enterocolitis, Journal of theoretical biology 321 (2013) 83–99. doi:10.1016/j.jtbi.2012.12.002.

[27] L. Caudill, F. Lynch, A Mathematical Model of the Inflammatory Response to Pathogen Challenge, Bulletin of Mathematical Biology 80 (Jun. 2018). doi:10.1007/s11538-018-0459-6.

[28] R. Leander, S. Dai, L. S. Schlesinger, A. Friedman, A Mathematical Model of CR3/TLR2 Crosstalk in the Context of Francisella tularensis Infection, PLOS Computational Biology 8 (11) (2012) e1002757. doi:10.1371/journal.pcbi.1002757.

[29] A. Waheed, A. Nazir, S. Ahmed, M. Zeb, N. Ahmed, U. Khan, M.-D. S. Tauseef, On conformable mathematical model of immune system coupled with intestinal microbiome, Thermal Science 23 (Suppl. 6) (2019) 2193–2198.

[30] H. Kettle, P. Louis, H. J. Flint, Process-based modelling of microbial community dynamics in the human colon, Journal of The Royal Society Interface 19 (195) (2022) 20220489. doi:10.1098/rsif.2022.0489.

[31] F. Blachier, M. Andriamihaja, P. Larraufie, E. Ahn, A. Lan, E. Kim, Production of hydrogen sulfide by the intestinal microbiota and epithelial cells and consequences for the colonic and rectal mucosa, American Journal of Physiology-Gastrointestinal and Liver Physiology 320 (2) (2021) G125–G135. doi:10.1152/ajpgi.00261.2020.

[32] S. W. Ragsdale, E. Pierce, Acetogenesis and the Wood-Ljungdahl Pathway of CO2 Fixation, Biochimica et biophysica acta 1784 (12) (2008) 1873–1898. doi:10.1016/j.bbapap.2008.08.012.

[33] B. Chassaing, J. D. Aitken, M. Malleshappa, M. Vijay-Kumar, Dextran Sulfate Sodium (DSS)-Induced Colitis in Mice, Current protocols in immunology / edited by John E. Coligan ... [et al.] 104 (2014) Unit–15.25. doi:10.1002/0471142735.im1525s104.

[34] C. Keribin, G. Celeux, V. Robert, The latent block model: A useful model for high dimensional data, in: ISI 2017-61st World Statistics Congress, 2017, pp. 1–6.

[35] J.-B. Leger, Blockmodels: A R-package for estimating in Latent Block Model and Stochastic Block Model, with various probability functions, with or without covariates (Feb. 2016). arXiv:1602.07587, doi:10.48550/arXiv.1602.07587.

[36] S. Y. Geerlings, I. Kostopoulos, W. M. de Vos, C. Belzer, Akkermansia muciniphila in the Human Gastrointestinal Tract: When, Where, and How?, Microorganisms 6 (3) (2018) 75. doi:10.3390/microorganisms6030075.

[37] X. Liu, B. Mao, J. Gu, J. Wu, S. Cui, G. Wang, J. Zhao, H. Zhang, W. Chen, Blautia—a new functional genus with potential probiotic properties?, Gut Microbes 13 (1) (2021) 1875796. doi:10.1080/19490976.2021.1875796.

[38] E. Salvetti, S. Torriani, G. E. Felis, The Genus Lactobacillus: A Taxonomic Update, Probiotics and Antimicrobial Proteins 4 (4) (2012) 217–226. doi:10.1007/s12602-012-9117-8.

[39] H. C. Mirsepasi-Lauridsen, B. A. Vallance, K. A. Krogfelt, A. M. Petersen, Escherichia coli Pathobionts Associated with Inflammatory Bowel Disease,

Clinical Microbiology Reviews 32 (2) (2019) e00060–18. doi:10.1128/CMR.00060-18.

[40] L. Darrigade, M. Haghebaert, C. Cherbuy, S. Labarthe, B. Laroche, A PDMP model of the epithelial cell turn-over in the intestinal crypt including microbiota-derived regulations, Journal of Mathematical Biology 84 (7) (2022) 60. doi:10.1007/s00285-022-01766-8.

[41] D. E. Contois, Kinetics of Bacterial Growth: Relationship between Population Density and Specific Growth Rate of Continuous Cultures, Microbiology 21 (1) (1959) 40–50. doi:10.1099/00221287-21-1-40.

[42] J. Monod, The Growth of Bacterial Cultures, Annual Review of Microbiology 3 (1) (1949) 371–394. doi:10.1146/annurev.mi.03.100149.002103.

[43] N. Gasaly, M. A. Hermoso, M. Gotteland, Butyrate and the Fine-Tuning of Colonic Homeostasis: Implication for Inflammatory Bowel Diseases, International Journal of Molecular Sciences 22 (6) (2021) 3061. doi:10.3390/ijms22063061.

[44] W. Babidge, S. Millard, W. Roediger, Sulfides impair short chain fatty acid β-oxidation at acyl-CoA dehydrogenase level in colonocytes: Implications for ulcerative colitis, Molecular and Cellular Biochemistry 181 (1) (1998) 117–124. doi:10.1023/A:1006838231432.

[45] J. H. Cummings, E. W. Pomare, W. J. Branch, C. P. Naylor, G. T. Macfarlane, Short chain fatty acids in human large intestine, portal, hepatic and venous blood., Gut 28 (10) (1987) 1221–1227. doi:10.1136/gut.28.10.1221.

[46] D. Aregba-Driollet, R. Natalini, S. Tang, Explicit diffusive kinetic schemes for nonlinear degenerate parabolic systems, Mathematics of Computation 73 (245) (2003) 63–94. doi:10.1090/S0025-5718-03-01549-7.

[47] R. Bravo, D. E. Axelrod, A calibrated agent-based computer model of stochastic cell dynamics in normal human colon crypts useful for in silico experiments, Theoretical Biology and Medical Modelling 10 (1) (2013) 66. doi:10.1186/1742-4682-10-66.

[48] H. Kettle, P. Louis, G. Holtrop, S. H. Duncan, H. J. Flint, Modelling the emergent dynamics and major metabolites of the human colonic microbiota, Environmental Microbiology 17 (5) (2015) 1615–1630. doi:10.1111/1462-2920.12599.

[49] D. R. Halm, S. T. Halm, Secretagogue response of goblet cells and columnar cells in human colonic crypts, American Journal of Physiology. Cell Physiology 278 (1) (2000) C212–233. doi:10.1152/ajpcell.2000.278.1.C212.